

Lagrangian Volume Deformations around Simulated Galaxies

S. Robles^{1*}, R. Domínguez-Tenreiro^{1,2}, J. Oñorbe³ and F.J. Martínez-Serrano^{4,5}

¹*Departamento de Física Teórica, Universidad Autónoma de Madrid, E-28049 Cantoblanco, Madrid, Spain*

²*Astro-UAM, UAM, Unidad Asociada CSIC*

³*Max-Planck-Institut für Astronomie, Königstuhl 17, D-69117, Heidelberg, Germany*

⁴*Dept. de Física y A.C., Universidad Miguel Hernández, E-03202 Elche, Spain*

⁵*Next Limit Dynamics SL, E-28048, Madrid, Spain*

Accepted 2015 April 12. Received 2015 March 30; in original form 2014 October 20

ABSTRACT

We present a detailed analysis of the local evolution of 206 Lagrangian Volumes (LVs) selected at high redshift around galaxy seeds, identified in a large-volume Λ cold dark matter (Λ CDM) hydrodynamical simulation. The LVs have a mass range of $1 - 1500 \times 10^{10} M_{\odot}$. We follow the dynamical evolution of the density field inside these initially spherical LVs from $z = 10$ up to $z_{\text{low}} = 0.05$, witnessing highly non-linear, anisotropic mass rearrangements within them, leading to the emergence of the *local* cosmic web (CW). These mass arrangements have been analysed in terms of the reduced inertia tensor I_{ij}^r , focusing on the evolution of the principal axes of inertia and their corresponding eigendirections, and paying particular attention to the times when the evolution of these two structural elements declines. In addition, mass and component effects along this process have also been investigated. We have found that deformations are led by dark matter dynamics and they transform most of the initially spherical LVs into prolate shapes, i.e. filamentary structures. An analysis of the individual freezing-out time distributions for shapes and eigendirections shows that first most of the LVs fix their three axes of symmetry (like a skeleton) early on, while accretion flows towards them still continue. Very remarkably, we have found that more massive LVs fix their skeleton earlier on than less massive ones. We briefly discuss the astrophysical implications our findings could have, including the galaxy mass-morphology relation and the effects on the galaxy-galaxy merger parameter space, among others.

Key words: gravitation – hydrodynamics – methods: numerical – galaxies: formation – cosmology: theory – large-scale structure of Universe

1 INTRODUCTION

Over the last few decades, galaxy surveys such as the Two-degree-Field Galaxy Redshift Survey (2dFGRS; Colless et al. 2001), the Sloan Digital Sky Survey (SDSS; e.g. Tegmark et al. 2004), the Two-Micron All-Sky Survey (2MASS; Huchra et al. 2005) and the 6dFGS (Jones et al. 2004) have revealed that galaxies gather in an intricate network, the so-called cosmic web (CW, after Bond, Kofman, & Pogosyan 1996), made of filaments, walls, nodes which surround vast empty regions, the voids (Zel’dovich 1970; Shandarin & Zeldovich 1989). These structures can be found on scales from a few to hundreds of megaparsecs and include huge flat structures like the Great Wall (Geller & Huchra 1989) and the SDSS Great Wall (Gott et al. 2005), the largest known structure in the local Universe, with a size larger than $400 h^{-1}$ Mpc and enormous empty regions like the Boötes void (Kirshner et al. 1981, 1987).

These results have been complemented by mappings of the dark matter (DM) spatial distribution through weak lensing obser-

vations like the Hubble Space Telescope Cosmic Evolution Survey (COSMOS; Massey et al. 2007) and recent results from the Canada–France–Hawaii Telescope Lensing Survey (CFHTLenS; Van Waerbeke et al. 2013).

Summing up, analyses of the current large scale distribution of galaxies and mass show that both are hierarchically organised into a highly interconnected network, displaying a wealth of structures and substructures over a huge range of densities and scales. This web can be understood as the main feature of the anisotropic nature of gravitational collapse (Peebles 1980), as well as of its intrinsic hierarchical character, and in fact it is the main dynamical engine responsible for structure formation in the Universe (Sheth 2004; Sheth & van de Weygaert 2004; Shen et al. 2006), including galaxy scales (Domínguez-Tenreiro et al. 2011).

According to the standard model of cosmology, large-scale structures observed in the Universe today are seeded by infinitesimal primordial density and velocity perturbations. The physical processes underlying their dynamical development until the CW emergence can be explained by theories and models on the gravitational instability, later on corroborated by a profusion of cosmolog-

* E-mail: sandra.robles@uam.es (SR)

ical simulations, the first of them purely N -body simulations (see e.g., Yepes, Domínguez-Tenreiro & Couchman 1992; Jenkins et al. 1998; Pogosyan et al. 1998; Colberg, Krughoff & Connolly 2005; Springel et al. 2005; Dolag et al. 2006), while recent ones include baryons and stellar physics too (see e.g., Domínguez-Tenreiro et al. 2011; Metuki et al. 2015).

Indeed, the advanced non-linear stages of gravitational instability are described by the Adhesion Model (AM; see Gurbatov & Saichev 1984; Gurbatov, Saichev & Shandarin 1989; Shandarin & Zeldovich 1989; Gurbatov, Malakhov & Saichev 1992; Vergasola et al. 1994 and Gurbatov, Saichev & Shandarin 2012, for a recent review), an extension of the popular non-linear Zeldovich Approximation (hereafter ZA; see Zel'dovich 1970). In comoving coordinates the ZA can be expressed as a mapping from the Lagrangian space (the space of initial conditions \vec{q}) into the Eulerian space (real space) described as a translation by a generalised irrotational velocity-like vector (the displacement field $\vec{s}(\vec{q})$) times the linear density growth factor $D_+(t)$, where the displacement can be written as a scalar potential gradient $\vec{s}(\vec{q}) = -\nabla_{\vec{q}}\Psi(\vec{q})$. This approximation allows us to predict where singularities (locations with infinite density) will appear as cosmic evolution proceeds (i.e., the \vec{q} points where the map has a vanishing determinant of the Jacobian matrix) and how they evolve into a sequence of caustics in real space. In this way, the ZA correctly but roughly describes the emergence of multistream flow regions, caustics and the structural skeleton of the CW (Doroshkevich, Ryaben'kii, & Shandarin 1973; Buchert 1989, 1992; Shandarin & Zeldovich 1989; Coles, Melott, & Shandarin 1993; Melott, Pellman, & Shandarin 1994; Melott, Shandarin, & Weinberg 1994; Melott, Buchert, & Weib 1995; Sahni & Coles 1995; Yoshisato, Matsubara, & Morikawa 1998; Yoshisato, Morikawa, Gouda, & Mouri 2006).

It is well known, however, that the ZA is not applicable once a substantial fraction of the mass elements are contained in multistream regions, because it predicts that caustics thicken and vanish due to multistreaming soon after their formation. One way of overcoming this issue is to introduce a small diffusion term in Zeldovich momentum equation, in such a way that it has an effect only when and where particle crossings are about to take place. This can be accomplished by introducing a non-zero viscosity, ν , and then taking the limit $\nu \rightarrow 0$: this is the AM, whose main advantage is that the momentum equation looks like the Burgers' equation (Burgers 1974) in the same limit, and hence its analytical solutions are known. A physically motivated derivation of the AM can be found in Buchert & Domínguez (1998); Buchert, Domínguez & Pérez-Mercader (1999); Buchert & Domínguez (2005).

The AM implies that, at a given scale, walls, filaments and nodes (i.e., the cosmic web elements) are successively formed, and then they vanish due to mass piling-up around nodes, to where mass elements travel through walls and filaments¹. Meanwhile, the same web elements emerge at larger and larger scales, and are erased at these scales after some time. Therefore, the AM conveniently describes both the anisotropic nature of gravitational collapse and the hierarchical nature of the process. In addition, the AM indicates that the advanced stages of non-linear evolution act as a kind of smoothing procedure on different scales, by wiping mass accumulations off walls and filaments, first at small scales and later on at successively larger ones, to the advantage of nodes. Another impli-

cation of the AM is that node centres (protohaloes at high z) lie on the former filaments at any z .

A very interesting achievement of the AM is that the first successful reduction of the cosmic large scale structure to a geometrical skeleton was done in this approximation (Gurbatov, Saichev & Shandarin 1989; Kofman, Pogosyan & Shandarin 1990; Gurbatov, Saichev & Shandarin 2012), see also Hidding, Shandarin & van de Weygaert (2014). Later on Novikov, Colombi & Doré (2006); Sousbie et al. (2008a,b); Sousbie, Colombi & Pichon (2009); Sousbie (2011); Sousbie, Pichon & Kawahara (2011); Aragón-Calvo, van de Weygaert & Jones (2010) and Aragón-Calvo et al. (2010) also discussed the skeleton or spine of large-scale structures from purely topological constructions in a given density field.

Recently, a growing interest to identify and analyse elements of the CW in N -body simulations, as well as in galaxy catalogues, has led to the development of different mathematical tools (Stoica et al. 2005; Aragón-Calvo et al. 2007a,b, 2010; Hahn et al. 2007b,a; Platen, van de Weygaert & Jones 2007; Stoica, Martínez & Saar 2007; Forero-Romero et al. 2009; Wu, Batuski & Khalil 2009; Aragón-Calvo, van de Weygaert & Jones 2010; Bond, Strauss & Cen 2010a,b; Genovese et al. 2012; González & Padilla 2010; Jones, van de Weygaert & Aragón-Calvo 2010; Stoica, Martínez & Saar 2010; Hoffman et al. 2012; Cautun, van de Weygaert & Jones 2013; Tempel et al. 2014). These methods and algorithms are motivated by the study of the influence of large scale structures on galaxy formation (Altay, Colberg & Croft 2006; Aragón-Calvo et al. 2007b; Hahn et al. 2007b,a; Paz, Stasyszyn & Padilla 2008; Hahn et al. 2009; Zhang et al. 2009; Godlowski, Panko & Flin 2011; Codis et al. 2012; Libeskind et al. 2012, 2013; Aragón-Calvo & Yang 2014; Metuki et al. 2015). In a recent paper, Cautun et al. (2014) have investigated the evolution of the CW from cosmological simulations, focusing on the global evolution of their morphological components and their halo content.

From a dynamical point of view, Hidding, Shandarin & van de Weygaert (2014) go a step further by establishing the link between the skeleton or spine of the CW, as described by the previous methods, and the development of the density field. In fact, they describe for the first time the details of caustic emergence as cosmic evolution proceeds. Their main result is to show that all dynamical processes related to caustics happen at locations placed near a set of critical lines in Lagrangian space, that, when projected onto the Eulerian space, imply an increasing degree of connectedness among initially disjoint mass accumulations in walls or filaments, until a percolated structure forms, i.e., the spine or skeleton of the large scale mass distribution. These authors compare their results with two dimensional N -body simulations. Note that, due to the complexity of the problem, they first work in two dimensional spaces, where caustic emergence and percolation are described. Nevertheless, they expect no important qualitative differences when three-dimensional spaces are considered instead.

As we can see, in the last years different methods to quantify the cosmic web structure, classify its elements and study its emergence and evolution have been developed and applied. However, a detailed analysis of the *local* development of the density field around galaxy hosting haloes is still missing. This is of major importance because of its close connection to the problem of galaxy formation, in which case the effects of including gas processes need to be considered too. It is worth noting that neither the ZA nor the AM include gas effects in their description of CW dynamics.

This analysis should first answer to the simplest questions related to *local* shape deformation and spine emergence and the orientation of its main directions or symmetry axes around galaxy-to-

¹ Recently confirmed in detail through CW element identification in large volume N -body simulations by Cautun et al. (2014).

be objects. Besides, the very nature of these *local* processes, there are other interesting, simple, not-yet-elucidated related issues. For instance the characterisation of the times when deformation stops and orientation gets frozen, whether or not this local web evolution is mass dependent (i.e., the mass of the halo-to-be) or not, and if different components (DM, hot gas, cold baryons) evolve in a similar way or there is a component segregation. We do not have at our disposal an analytical tool to perform such analyses, in consequence we need to resort to numerical simulations.

In order to answer these questions, in this paper we investigate the impact of the local features of the Hubble flow imprinted on the deformation of initially spherical Lagrangian volumes (LVs) and the spine emergence, from high to low redshift. As known from previous studies, the local Hubble flow is neither homogeneous nor isotropic, on the contrary, it contains shear terms (and small-scale vorticity at its most advanced stages) that distort cosmological structures. We use cosmological hydrodynamical simulations to study the deformations of a sample of LVs through their reduced inertia tensor at different redshifts, which allows us to describe in a quantitative way the LV shape deformation and evolution, along with that of their symmetry axes. We analyse every component separately, that is, we compute the reduced inertia tensor for DM, cold and hot baryons.

This paper is organised as follows. In §2, we outline the simulation method and the algorithms used to study the deformations of LVs. A brief summary on the ZA, the CW emergence in 2D and the AM is given in §3, where some of their implications, useful in this paper, are also addressed. Some relevant details of the highly non-linear stages of gravitational instability, beyond the ZA or the AM are summarised in §4, to help to understand how our results about the LV evolution can be explained in the light of these models. In §5, the LV evolution is investigated in terms of the reduced inertia tensor eigenvectors, delaying the analysis in terms of its eigenvalues to the next section, §6, focused on the mass and component effects and on the shape evolution of the selected LVs. In §7 we study the freezing-out of eigendirections and shapes, presenting the distribution of the corresponding freezing-out times and looking for mass effects. Possible scale effects on the previous results are discussed in §8. Finally, we present our summary, conclusions and discussion in §9.

2 SIMULATIONS AND METHODS

2.1 Simulations

The simulations analysed here have been run under the GALFOBS I and II projects. The GALFOBS (Galaxy Formation at Different Epochs and in Different Environments: Comparison with Observational Data) project aims to study the generic statistical properties of galaxies in various environments and at different cosmological epochs. This project was a DEISA Extreme Computing Initiative (DECI)². GALFOBS I was run at LRZ (Leibniz-Rechenzentrum) Munich, as a European project. Its continuation, GALFOBS II, was run at the Barcelona Supercomputing Centre, Spain.

All the runs were performed using P-DEVA, the parallelised version of the DEVA code (Serna, Domínguez-Tenreiro & Sáiz 2003). DEVA is an hybrid AP³M Lagrangian code, implemented

with a multistep algorithm and smoothed particle hydrodynamics (SPH). The SPH version included in P-DEVA ensures energy and entropy conservation and, at the same time, guarantees a good description of the forces and angular momentum conservation. However, this advantage implies a gain in accuracy and an additional computational cost. Star formation (SF) is implemented through a Kennicutt–Schmidt-like law with a given density threshold, ρ_* , and star formation efficiency c_* (Martínez-Serrano et al. 2008).

The simulations have been carried out in the same periodic box of 80 Mpc side length, using 512^3 baryonic and 512^3 DM particles. Due to computational cost, these simulations only include hydrodynamical calculation in a sub-box of 40 Mpc side. The evolution of matter follows the Λ cold dark matter (Λ CDM) model, with parameters $\Omega_m = 0.295$, $\Omega_b = 0.0476$, $\Omega_\Lambda = 0.705$, $h = 0.694$, an initial power-law index $n = 1$, and $\sigma_8 = 0.852$, taken from cosmic microwave background anisotropy data³ (Dunkley et al. 2009). The star formation parameters used were a density threshold $\rho_{thres} = 4.79 \times 10^{-25} \text{ g cm}^{-3}$ and a star formation efficiency $c = 0.3$. The mass resolution is $m_{bar} = 2.42 \times 10^7 M_\odot$ and $m_{DM} = 1.26 \times 10^8 M_\odot$ and a spatial resolution of 1.1 kpc in hydrodynamical forces. More detailed information of these simulations can be found in Oñorbe et al. (2011).

It is noteworthy that no explicit feedback has been implemented in these simulations, but SF regulation through the values of the SF parameters. Nevertheless, the issues that will be discussed in this paper involve considerably larger characteristic scales than the ones related to stellar feedback. Therefore, it is unlikely that the details of the star formation rate, and those of stellar feedback in particular, could substantially alter the conclusions of this paper.

2.2 Methods

We first describe how the LV sample around simulated galaxies has been built up. The first step is halo selection at $z_{low} = 0.05$ by using the SKID algorithm⁴ (Weinberg, Hernquist & Katz 1997). This multi-step algorithm determines first the smoothed density field, then it moves particles upward along the gradient of this density field using a heuristic equation of motion that forces them to collect at local density maxima. Afterwards, it defines the approximate group to be the set of particles identified with an FOF algorithm with a linking length, b . Finally, particles not gravitationally bound to the groups identified in the previous step are removed.

Specifically, we have selected a sample of 206 galaxy haloes from two runs of the GALFOBS simulations at z_{low} , not involved in violent events at the halo scale at z_{low} . Their virial radii $r_{vir,low}$ and masses $M_{vir,low}$ at this redshift go from dwarf galaxies to galaxy groups, see the corresponding histograms in Fig. 1 first row. The virial radius (r_{vir}) is defined as the radius of the sphere enclosing an overdensity given by Bryan & Norman (1998).

Next, for each halo at z_{low} we have traced back all the particles inside the sphere defined by its respective $r_{vir,low}$ to $z_{high} = 10$. Using the position of these particles at z_{high} we have calculated a new centre \vec{r}_c . Then, we have selected at z_{high} all the particles enclosed by a sphere of radius $R_{high} = K \times r_{vir,low}$, with $K = 10$ around their respective centres \vec{r}_c (see first row of Fig. 2), and we have identified each of the DM and baryonic particles within these spherical volumes. These particles sample the mass elements

² The DEISA Extreme Computing Initiative was launched in May 2005 by the DEISA Consortium, as a way to enhance its impact on science and technology

³ http://lambda.gsfc.nasa.gov/product/map/dr3/params/lcdm_sz_lens_run_wmap5_bao_snall_lyapost.cfm

⁴ <http://www-hpcc.astro.washington.edu/tools/skid.html>

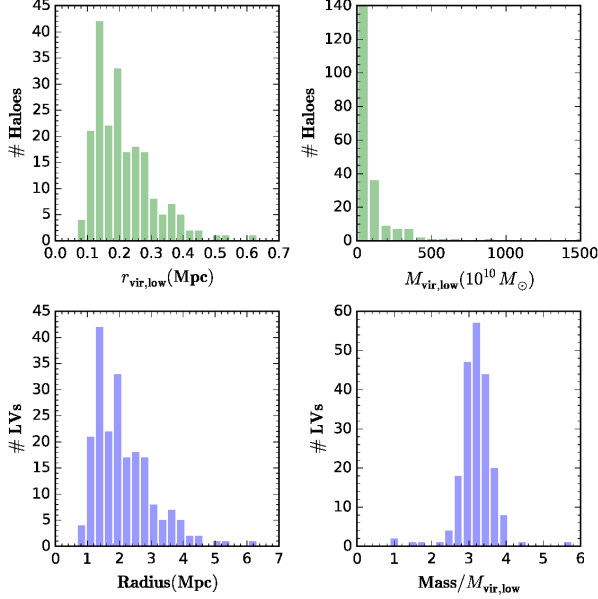


Figure 1. Upper panels show the radius and mass distribution of the galaxy haloes at z_{low} in our sample. Lower panels depict the same information for the selected LVs.

whose deformations, stretchings, foldings, collapse and stickings we are to trace along cosmic evolution. They follow geodesic trajectories until they possibly get stuck and begin the formation of, or are accreted onto, a CW structure element. For this reason, we have termed them Lagrangian Volumes (LVs). It is worth noting at this point that we are following the evolution of individual LVs, each of them made of a fixed number of particles as they evolve. We do not trace the possible incorporation of off-LV mass elements that could happen along evolution as a consequence of mergers, infalls or other processes. Note also that, due to the very complex evolution of the LVs, their borders are not well defined at $z < z_{\text{high}}$. Finally, a technical point to take into account is that the LVs should lie inside the hydrodynamical zoomed box.

The choice $K = 10$ is motivated as a compromise between low K values, ensuring a higher number of LVs in the sample, and a high K , ensuring that LVs are large enough to meaningfully sample the CW emergence around forming galaxies. The possible effects that different K values could have in our results will be discussed in Section 8, where we conclude that $K = 10$ is the best choice among the three possibilities analysed.

Afterwards, we have followed the dynamical evolution of these particles across different redshifts until they reach z_{low} , i.e., we have followed the evolution (stretchings, deformations, foldings, collapse, stickings) of a set of 206 LVs from z_{high} until z_{low} . By construction, the mass of each of these sets of particles is constant across evolution, and its distribution is given in Fig. 1, second row, where we also show the distribution of their initial sizes at z_{high} .

The choice of initially *spherically* distributed sets of particles aims to unveil the anisotropic nature of the local cosmological evolution, illustrated in Fig. 2, where two examples of LVs at $z = 10$ and their corresponding final shapes and orientations at z_{low} are displayed. The mass of these LVs are $8.7 \times 10^{12} M_{\odot}$ (left-hand panels) and $4.4 \times 10^{12} M_{\odot}$ (right-hand panels), respectively.

In this figure we note that, in both cases, a massive galaxy

appears at z_{low} in the central region of the LV. It turns out that, by construction, these galaxies are just those identified in the first step of the LV sample building-up, see above. We also notice that the LVs have evolved into a highly irregular mass organisation, including very dense subregions as well as other much less dense and even rarefied ones. Also, some changes of orientation of the emerging spines are visible, mainly in the lighter LV. In addition, the initial cold gaseous configuration at $z = 10$ has been transformed into a system where stars (in blue) appear at the densest subregions of the LVs. Hot gas (in red) particles are also present and constitute an important fraction of the LV mass (see §4 for an explanation about its origin). We also observe that the overall LV shape on the right-hand side of Fig. 2 is highly elongated at z_{low} and has a prolate-like or filamentary appearance, visually spanning a linear scale of ~ 9 Mpc long by 2 Mpc wide, while that on the left-hand side of Fig. 2 still keeps a more wall-like structure. These shape transformations illustrate the highly anisotropic character of evolution under gravity. In this respect, it is worth mentioning that anisotropy is a generic property of gravitational collapse for non-isolated systems, as it was pointed out in early works by Lin, Mestel & Shu (1965); Icke (1973) and White & Silk (1979).

As we mentioned in §1, the deformation, stretching, folding, multistreaming and collapse of mass elements by cosmological evolution is predicted and described by the ZA, while AM adds a viscosity term making multistreaming regions to get stuck into dense configurations. In the following, we will introduce the mathematical methods we use to quantify the local LV transformations illustrated in Fig. 2.

To this end, we have calculated, at different redshifts, the reduced inertia tensor of each LV relative to its centre of mass

$$I_{ij}^r = \sum_n m_n \frac{(\delta_{ij} r_n^2 - r_{i,n} r_{j,n})}{r_n^2}, \quad n = 1, \dots, N \quad (1)$$

where r_n is the distance of the n -th LV particle to the LV centre of mass and N is the total number of such particles. We have used this tensor instead of the usual one (Porciani, Dekel & Hoffman 2002a) to minimise the effect of substructure in the outer part of the LV (Gerhard 1983; Bailin & Steinmetz 2005). In addition, the reduced inertia tensor is invariant under LV mass rearrangements in radial directions relative to the LV centre of mass. This property makes the I_{ij}^r tensor particularly suited to describe anisotropic mass deformations as those predicted by the ZA and the AM and observed in Fig. 2.

In order to measure the LV shape evolution, first, we have calculated the principal axes of the inertia ellipsoid, a , b , and c , derived from the eigenvalues (λ_i , with $\lambda_1 \leq \lambda_2 \leq \lambda_3$) of the I_{ij}^r tensor, so that $a \geq b \geq c$ (see González-García & van Albada (2005)),

$$a = \sqrt{\frac{5(\lambda_2 - \lambda_1 + \lambda_3)}{2M}}, \quad b = \sqrt{\frac{5(\lambda_3 - \lambda_2 + \lambda_1)}{2M}}, \quad (2)$$

$$c = \sqrt{\frac{5(\lambda_1 - \lambda_3 + \lambda_2)}{2M}},$$

where M is the total mass of a given LV⁵. We denote the directions of the principal axes of inertia by \hat{e}_i , $i = 1, 2, 3$, where \hat{e}_1 correspond to the major axis, \hat{e}_2 to the intermediate one and \hat{e}_3 to the minor axis.

Afterwards, to quantify the deformation of these LVs, we have

⁵ Note that $\lambda_1 + \lambda_2 + \lambda_3 = 2M$ and this implies $a^2 + b^2 + c^2 = 5$.

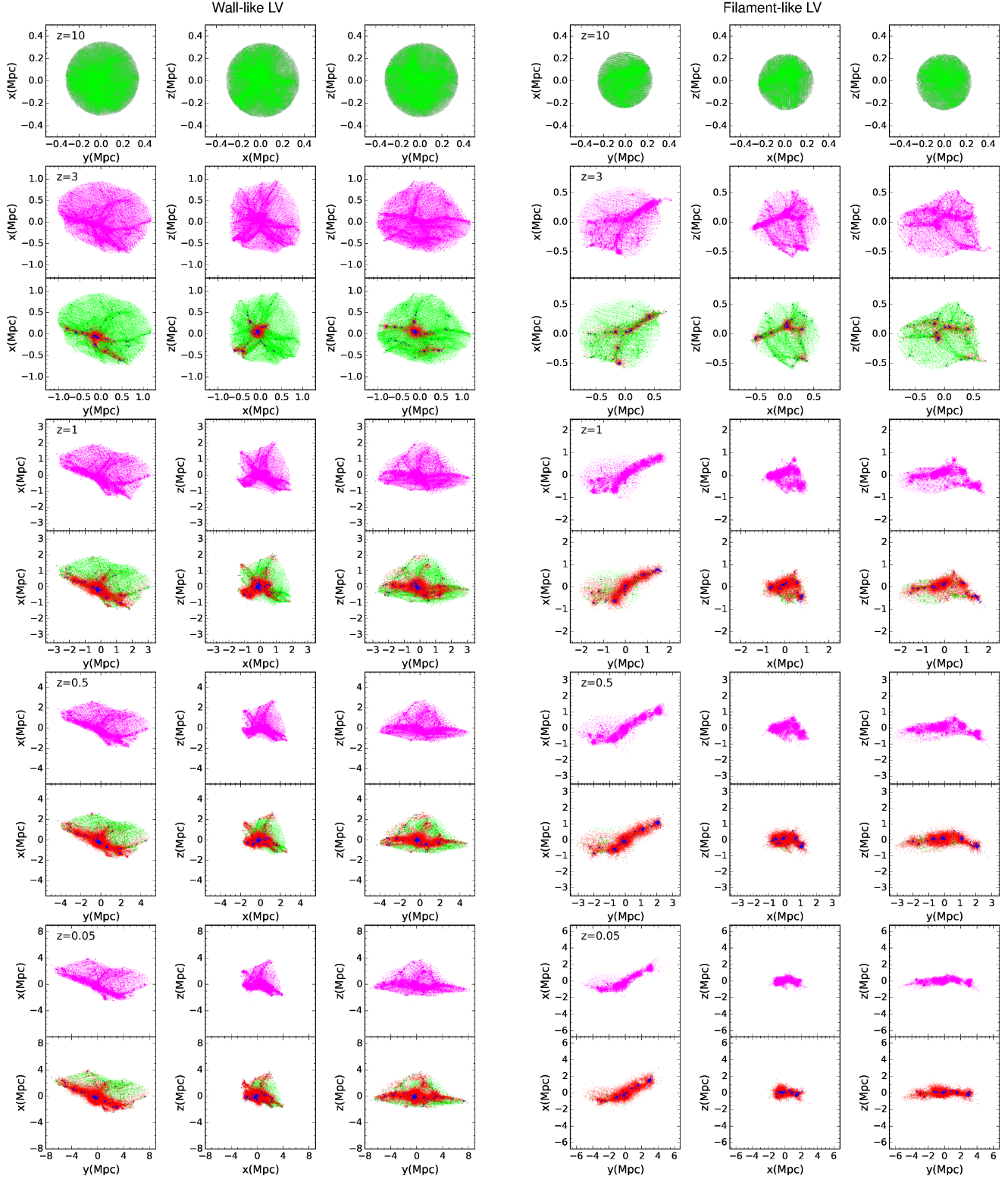


Figure 2. Left. shape evolution of a wall-like LV from $z = 10$ to $z_{\text{low}} = 0.05$. Different columns are three projections of the same LV, with fixed axes taken oriented along the direction of the principal axes at z_{low} . Magenta points represent DM, green cold gas, red hot gas ($T \geq 3 \times 10^4$ K) and blue stars. First row shows the initially spherical LV at $z = 10$, where DM and cold gas are represented in the same plot. Second, third, fourth and fifth group of panels illustrate the LV shape deformation across redshifts $z = 3, 1, 0.5$ and 0.05 , where DM and baryonic components are split in different rows. Right. the same for a filament-like LV. The mass of the LVs are $8.7 \times 10^{12} M_{\odot}$ and $4.4 \times 10^{12} M_{\odot}$, respectively.

computed the triaxiality parameter, T , (Franx, Illingworth & de Zeeuw 1991), defined as

$$T = \frac{(1 - b^2/a^2)}{(1 - c^2/a^2)}, \quad (3)$$

where $T = 0$ corresponds to an oblate spheroid and $T = 1$ to a prolate one. An object with axis ratio $c/a > 0.9$ has a nearly spheroidal shape, while one with $c/a < 0.9$ and $T < 0.3$ has an oblate triaxial shape. On the other hand, an object with $c/a < 0.9$ and $T > 0.7$ has a prolate triaxial shape (González-García et al. 2009).

We have also calculated other parameters that measure shape deformation such as, ellipticity, e

$$e = \frac{a^2 - c^2}{a^2 + b^2 + c^2}, \quad (4)$$

that quantifies the deviation from sphericity, and prolateness, p

$$p = \frac{a^2 + c^2 - 2b^2}{a^2 + b^2 + c^2}, \quad (5)$$

that compares the prolateness versus the oblateness (Bardeen et al. 1986; Porciani, Dekel & Hoffman 2002b; Springel, White & Hernquist 2004). In this case, a sphere has $e = p = 0$, a circular disc has $e = 0.5$, $p = -0.5$ and a thin filament has $e = p = 1$. Nearly spherical objects have $e < 0.2$ and $|p| < 0.2$.

To sum up, we have performed the computation of the reduced inertia tensor, the principal axes of inertia, the eigendirections and the parameters T , e and p involving each of the selected LVs. Furthermore, we have repeated the same calculation for each component separately, viz. DM, cold and hot baryons. We consider hot gas as the particles shock heated to 3×10^4 K.

3 EVOLUTION UNDER THE ZA OR THE AM

The advanced non-linear stages of gravitational instability are described by the *adhesion model* (Gurbatov & Saichev 1984; Gurbatov, Saichev & Shandarin 1989; Shandarin & Zeldovich 1989; Gurbatov, Malakhov & Saichev 1992; Vergassola et al. 1994), an extension of Zeldovich's (1970) popular non-linear approximation. In this Section, we briefly revisit them as well as some of their implications, useful to understand the results that will be analysed in the next sections.

3.1 The Zeldovich Approximation

In comoving coordinates, Zeldovich's approximation is given by the so-called *Lagrangian map*:

$$x_i(\vec{q}, t) = q_i + D_+(t)s_i(\vec{q}), \quad (6)$$

where q_i and x_i , $i = 1, 2, 3$ are comoving Lagrangian and Eulerian coordinates of fluid elements or particles sampling them, respectively (i.e., initial positions at time t_{in} and positions at later times t); $D_+(t)$ is the linear density growth factor. As already mentioned, it turns out that $s_i(\vec{q})$ can be expressed as the gradient of the displacement potential $\Psi(\vec{q})$.

The behaviour of $D_+(t)$ depends on the cosmological epoch. For the flat concordance cosmological model (see § 2.1), at high enough z , when the Universe evolution is suitably described by the Einstein-de Sitter model, $D_+(t) = (3/5)(t/t_i)^{2/3}$. Later on, when $\frac{d^2a}{dt^2} \simeq 0$ and the effects of the cosmological constant emerge ($z_\Lambda \simeq 0.684$ or $t_\Lambda/t_U = 0.554$ for the cosmological model used in

the simulations analysed here), $D_+(t)$ is an exponential function of time. Finally, when the cosmological constant dominates, we have:

$$D_+(a(t)) \propto \mathfrak{B}_x(5/6, 2/3) \left(\frac{\Omega_0}{\Omega_\Lambda} \right)^{1/3} \left[1 + \frac{\Omega_M}{a^3 \Omega_\Lambda} \right]^{1/2}, \quad (7)$$

where \mathfrak{B}_x is the incomplete β function, $\Omega_0 = 1 - \Omega_\Lambda$, Ω_M is the non-relativistic contribution to Ω_0 , and

$$x \equiv \frac{a^3 \Omega_\Lambda}{\Omega_0 + a^3 \Omega_\Lambda}, \quad (8)$$

describing a frozen perturbation in the limit $t \rightarrow \infty$.

Due to mass conservation, equation 6 implies for the local density evolution:

$$\rho(\vec{r}, t) = \frac{\rho_b(t)}{[1 - D_+(t)\alpha(\vec{q})][1 - D_+(t)\beta(\vec{q})][1 - D_+(t)\gamma(\vec{q})]}, \quad (9)$$

where $\vec{r} = a(t)\vec{x}$ is the physical coordinate, $\rho_b(t)$ the background density, and $\gamma(\vec{q}) < \beta(\vec{q}) < \alpha(\vec{q})$ are the eigenvalues of the local deformation tensor, $d_{i,j}(\vec{q}) = -\left(\frac{\partial s_i}{\partial q_j}\right)_{\vec{q}}$. Equation 9 describes caustic formation in the ZA. Indeed, a caustic first appears when and where $D_+(t)\alpha(\vec{q}) = 1$ (i.e., a wall-like one), see details in § 3.2. Mathematically, caustics at time t can be considered as singularities in the *Lagrangian map* (see equation 6 and more details in the next subsection).

3.2 The CW Emergence in 2D

The emergence of the cosmic skeleton as cosmic evolution proceeds in the frame of the ZA is presented by Hidding, Shandarin & van de Weygaert (2014). Due to the high complexity of the formalism involved, the authors restrict themselves to the two-dimensional equivalent of the ZA, providing us with the concepts, principles, language and processes needed as a first step towards a complete dynamical analysis of the CW emergence in the full three-dimensional space. In this subsection we give a brief summary of some of their results, useful to interpret some of our findings.

In 2D, the complexity of the cosmic structure can be understood to a large extent from the properties of the $\alpha(\vec{q})$ landscape field, where $\alpha(\vec{q})$ is the largest eigenvalue of the deformation tensor $d_{i,j}(\vec{q})$, $i, j = 1, 2$. The role of the second eigenvalue $\beta(\vec{q})$ is much less relevant, except around the places where the haloes are to form.

Of particular relevance are the A_3 lines in Lagrangian space, because they are the progenitors of the cosmic skeleton in Eulerian space. Geometrically they can be defined as the locus of the points where the gradient of α (or β) eigenvalue is normal to its corresponding eigenvector \vec{e}_α (or \vec{e}_β). Alternatively, they can also be defined as the locus of the points where \vec{e}_α (or \vec{e}_β) is tangential to the contour level of the $\alpha(\vec{q})$ (or $\beta(\vec{q})$) landscape field.

The locations where collapse first occurs are around the maxima of the $\alpha(\vec{q})$ field in Lagrangian space. These are the so-called A_3^+ singularities, after Arnold's singularity classification (Arnold 1983). They are placed on the A_3 lines. Subsequently, the evolution under the ZA drives a gradual progression of Lagrangian collapsing regions, consisting, at a given time t , of those points such that $\alpha(\vec{q}) = 1/D_+(t)$ or $\beta(\vec{q}) = 1/D_+(t)$, according to the 2D version of equation 9. These isocontours lines are the so-called $A_2^\alpha(t)$ and $A_2^\beta(t)$ lines, and within them matter is multistreaming in Eulerian space, i.e., matter forms a fold caustic or pancake.

The height of the $\alpha(\vec{q})$ landscape field portrays the collapse time for a local mass element. Indeed, at a given time t , points

where the $A_2^\alpha(t)$ and the A_3^α lines meet, correspond to points in Eulerian space where a cusp singularity can be found (i.e., the tip of a caustic). The $A_2^\alpha(t)$ lines descend on the $\alpha(\vec{q})$ landscape field as time elapses, and in this way more and more mass elements get involved in the pancake. The pancake grows in Eulerian space, where the two cusp singularities at their tips move away from each other. A similar description can be made for the $\beta(\vec{q})$ eigenvalue.

Note that the height of either the $A_2^\alpha(t)$ or the $A_2^\beta(t)$ lines depends only on the $D_+(t)$ function, and not on the eigenvalue landscape fields. Therefore, the higher the $\alpha(\vec{q})$ landscape field, the earlier the corresponding pancake in the Eulerian space is formed. The same argument holds for the $\beta(\vec{q})$ eigenvalue.

Along the A_3 lines there are another types of extrema. First, we have the A_3^- singularities or saddle points, after Arnold's classification. They are in-between two A_3^+ singularities and are local minima along the A_3 lines. They depict the places where two pancakes emerging from each of the A_3^+ points get connected, when the corresponding A_2 lines met the A_3^- singularities at their descent. This represents a first percolation event, and a first step towards the emergence of the CW spine. For the aforementioned reasons, the higher the $\alpha(\vec{q})$ landscape field, the earlier the percolation events will occur.

The second type are the local maxima points \vec{q}_4 , where the corresponding eigenvector is tangent to the A_3 lines, i.e., the so-called A_4 singularities, or swallow tail according to Arnold (1983). An A_4 singularity at \vec{q}_4 exists only at a unique instant t_4 , when $\alpha(\vec{q}_4) = 1/D_+(t_4)$. At this moment, the $A_2^\alpha(t_4)$ line passes through A_4 , transforming the cusp singularity at the end of the Eulerian pancake into a swallow tail singularity. After that, there are three intersections of the $A_2(t)$ line with two A_3 lines, giving three connected cusp singularities in Eulerian space. Therefore, the A_4 singularities are the connection points where disjoint pieces of A_3 lines get connected in Eulerian space. Then, we get another percolation process. Once again, as explained above, the higher the $\alpha(\vec{q})$ landscape field, the earlier the percolation events will take place.

This short summary illustrates some aspects of the effect that the height of the $\alpha(\vec{q})$ landscape field has on the time when simple percolation events occur in 2D, or, in a more general scope, when the CW spine emerges. The conclusion is simple: the higher the eigenvalue landscape, the earlier the percolation events take place. A similar effect can be expected in 3D, provided that the description of the events connecting disjoint caustics in Eulerian space is not dramatically changed with respect to that in 2D.

Pancake formation in Eulerian space entails an anisotropic mass rearrangement as matter flows normally to the α (or β) pancake. These flows consist of mass elements within the $A_2^\alpha(t)$ (or $A_2^\beta(t)$) lines in Lagrangian space, and therefore they ideally do not stop while the A_2 lines keep on descending on the landscape. Similar ideas apply to other kind of caustic formation, implying shape transformations after the skeleton emergence. Note that matter flows are predominantly anisotropic, except for the places where the haloes are to form, i.e. where flows become more isotropic.

3.3 The Adhesion Model

As it is well known, Zeldovich's approximation is not applicable beyond particle crossing, because it predicts that caustics thicken and vanish due to multistreaming soon after their formation. However, N -body simulations of large-scale structure formation indicate that long-lasting pancakes are indeed formed, near which particles stick, i.e. multistreaming did not take place. The adhesion model was formulated to incorporate this feature to Zeldovich's ap-

proximation, by introducing a small diffusion term in Zeldovich's momentum equation, in such a way that it has an effect only when and where particle crossings are about to take place. This can be accomplished by introducing a non-zero viscosity, ν , and then taking the limit $\nu \rightarrow 0$. This is the phenomenological derivation of the adhesion model. Physically motivated derivations can be found in Buchert & Domínguez (1998), Buchert, Domínguez & Pérez-Mercader (1999) and others included in the review by Buchert & Domínguez (2005).

As in the Zeldovich approximation, in the adhesion model, the initial velocity field can be expressed as the gradient of a scalar potential field, $\Phi_0(\vec{q})$, describing the spatial structure of the initial perturbation. It can be shown that the solutions for the velocity field behave just as those of Burgers' equation (Burgers 1948, 1974) in the limit $\nu \rightarrow 0$, whose analytical solutions are known.

The most significant characteristic of Burgers' equation solutions is that they are discontinuous and hence they unavoidably develop singularities, i.e., locations where at a given time the velocity field becomes discontinuous and certain particles coalesce into *long-lasting* very dense configurations with different geometries, i.e., caustics as in the ZA. The ideas explained in § 3.2 also apply here, but the main difference is that matter gets stuck forming very dense subvolumes (singularities) in Eulerian space, instead of forming multistreaming regions. In this way, a singularity occurs at the time t when a non-zero d -dimensional elemental volume V around a point \vec{q} in the initial configuration is mapped to a d' -dimensional elemental volume around a point $\vec{x}(\vec{q}, t)$ in Eulerian space with $d' < d$. In a three-dimensional space, these singularities can be walls (with dimension $d' = 2$), filaments ($d' = 1$) and nodes ($d' = 0$).

The AM model implies that, locally, walls are the first singularities that appear, as denser small surfaces (the so-called pancakes). Later on, filaments form and grow until singularity percolation and spine emergence (Gurbatov, Saichev & Shandarin 1989; Kofman, Pogosyan & Shandarin 1990; Gurbatov, Saichev & Shandarin 2012). The singularity pattern implies the emergence of anisotropic mass flows towards the new formed singularities. Locally, emerging walls are the first that attract flows from voids, then they host flows towards filaments, and, finally, filaments are the paths of mass towards nodes. In this way, at a given scale, walls and filaments tend to vanish as the mass piles up at nodes. In addition, cells associated with the deepest minima of $-\Phi_0(\vec{q})$, swallow up some of their neighbouring cells related to less deep minima, involving their constituent elements (i.e., walls, filaments and nodes), and causing their merging, as in the ZA. This is observed in simulations as contractive flow deformations that erase substructure at small scales, as mentioned above, while the CW is still forming at larger scales.

It is worth noting that Burgers' equation solutions ensure the existence of *regular points or mass elements* at any time t , as those that have not yet been trapped into a caustic at t . Because of that, these regular mass elements are among the least dense in the density distribution. Note, however, that due to the complex structure of the flow, singular (i.e., already trapped into a caustic) and regular (i.e., not yet trapped) mass elements need not be spatially segregated, and in fact, they are mixed ideally at any scale.

3.4 Further implications

According to the ZA, we have

$$\nabla_{\vec{q}} \cdot \vec{s} \equiv \alpha(\vec{q}) + \beta(\vec{q}) + \gamma(\vec{q}) = \frac{5\delta\rho}{3\rho}(t_{in}). \quad (10)$$

As suggested by the 2D analysis made in § 3.2, the height of the $\alpha(\vec{q})$ landscape field in 3D portrays the collapse time for local mass elements (with $\alpha(\vec{q})$ the larger $d_{i,j}$ eigenvalue at \vec{q}), as well as the time when different percolation events mark the emergence of the CW spine. Equation 10 indicates that the eigenvalue landscape fields are closely related to the fluctuation field (FF) $\frac{\delta\rho}{\rho}$ at t_{in} .

It is well known that the number density of the FF peaks above a given threshold is considerably enhanced by the presence of a (positive) background field (Bardeen et al. 1986), or, equivalently, when a large-scale varying field is added to $\frac{\delta\rho}{\rho}$. Equation 10 tells us that such background would increase the height of the landscape fields, thereby speeding up percolation events responsible for the CW emergence. Note that denser LVs, when compared to less dense ones, can be considered as the result of adding a large-scale varying field to the latter. Consequently, we expect that the CW elements appear and percolate earlier on within denser LVs than within less dense ones.

These considerations apply to the evolution of the I_{ij}^r eigenvectors, $\hat{e}_i(z)$, and to their possible dependence on mass.

Regarding shape evolution, as already emphasised, mass anisotropically flows towards new singularities. These anisotropic mass arrangements make the I_{ij}^r eigenvalues evolve. Thus, evolution becomes gradually extinct as anisotropic flows tend to vanish. At small scales, the CW structure is swallowed up and removed by contractive deformations, see previous subsection. From a global point of view, the CW dynamic evolution somehow stops and the structure becomes frozen as $\frac{dD_+(t)}{dt} \rightarrow 0$, that is after the Λ term dominates the expansion at z_Λ , see equation 7. Therefore, matter flows are expected to become on average less and less relevant after z_Λ , as time elapses.

In addition, it is expected that locally the first to vanish are the flows associated with $\alpha(\vec{q})$, the largest eigenvalue of the local deformation matrix $d_{i,j}(\vec{q})$ (i.e. the flows towards walls), and the last to disappear are those flows related to $\gamma(\vec{q})$, the smallest deformation matrix $d_{i,j}(\vec{q})$ eigenvalue (i.e. the flows towards nodes).

Disentangling how these theoretical local predictions affect the global shape evolution of LVs demands numerical simulations. We will address these issues in the next sections.

4 EVOLUTION BEYOND THE ZA OR THE AM

Some concepts, not directly described by the ZA or the AM, need to be clarified in order to correctly explain Fig. 2 at a qualitative level, as well as some results to be discussed in forthcoming sections.

4.1 Caustic dressing

The phenomenological Adhesion Model tells nothing about the internal density or velocity structure of locations where mass gets adhered. Just to have a clue from theory, we recall that in his derivation of a generalised adhesion-like model, Domínguez (2000) found corrections to the momentum equation of the ZA that regularise (i.e., dress) its wall singularities. These then become long-lasting structures where more mass gets stuck, but within non-zero volumes supported by velocity dispersion coming from the energy transfer from ordered to disordered motions. (see also Gurbatov, Saichev & Shandarin 1989, for a discussion of these effects in terms of the viscosity, phenomenologically introduced in the AM). The analyses of N -body simulations strongly suggest that any kind of

flow singularity gets dressed (i.e., not only at pancakes, as it has been analytically proven by Domínguez 2000).

4.2 Gas in the cosmic web

When gas is added, the energy transfer from ordered to disordered motions around singular structures includes the transformation of velocity dispersion into internal gas energy (heating) and pressure. Then, energy is lost through gas cooling, mainly at the densest pieces of the CW, making them even denser. However, as already said in §3.3, singular (i.e., dense) and regular (i.e., not yet involved in singularities, low density) mass elements are mixed at any scale. Therefore, low-density gas is heated too, and, in addition, pressurised. The consequences of these processes cannot be deciphered from theory, but previous analyses of cosmological hydrodynamical simulations in terms of the CW (see, for example Domínguez-Tenreiro et al. 2011) suggest that dressing acts on any kind of flow singularity, i.e., also on filaments and nodes. Moreover, these authors conclude that, at (node-like) halo collapse, cooling of low-density gas is so slow that most gravitationally heated gas is kept hot until $z = 0$. In any case, because hot gas is pressurised, no anisotropic mass inflows towards singularities can be expected within the hot gas component, on the contrary, possible anisotropic, pressure-induced hot gas outflows are expected from them. These expectations will be explored in the following sections.

On the other hand, at the densest gas locations, cold gas is transformed into stars with an efficiency ϵ when the density is higher than a threshold. In this way, the hot gas component and the stars, observed in Fig. 2, arise.

4.3 A visual impression of LV evolution

Fig. 2 gives us a first visual impression of the evolution of the initially spherical LVs. The former considerations above make it easier a qualitative interpretation of what these figures show. Indeed, the gradual emergence of a local skeleton stands out in both of them, including web-element mergings and some rotations too. Finally, at z_{low} , we see an elongated structure, either in the DM, cold or hot baryonic components, where different spherical configurations appear, with a stellar component at the centre of most of them⁶. A high fraction of hot gas component (but not its whole mass) is related to these spheres. This complicated structure comes from wall and filament formation, according to the AM, and its dressing and eventual fragmentation into clumps. Clumps are in their turn dressed. Note also that, at each z , a fraction of the matter is not yet involved into singularities. Therefore, evolution leads to: (i) a DM component sharing both a diffuse and a dressed singularity configuration, with the particularity that the LV diffuse component present at redshift z has not yet been involved in any singularity at z , (ii) a complex cold gas component, sharing also a diffuse as well as a dressed singularity configuration, but with a more concentrated distribution than that of the DM, because gas can lose energy by radiation and (iii) a complex hot gas distribution. As explained in § 4.2, diffuse gas is gravitationally heated at collapse events, but, as will be shown in § 6.3, it is not involved in important anisotropic mass rearrangements.

To further advance, we need a quantitative analysis of LV evolution. This is the subject of the next sections.

⁶ We note that there is a component effect, namely different components (i.e. DM, cold and hot baryons) evolve dissimilarly.

5 ANISOTROPIC EVOLUTION: EIGENVECTORS OF THE MASS DISTRIBUTION

According to the AM, mass elements are anisotropically deformed and a fraction of them pass through one or several singularities in sticking regions. For each mass element placed at a Lagrangian point \vec{q} , accretion at high z preferentially occurs along the eigenvector corresponding to the largest eigenvalue of the symmetric deformation matrix at \vec{q} , $d_{i,j}(\vec{q}) = -\left(\frac{\partial s_i}{\partial q_j}\right)_{\vec{q}}$.

Taking the LV as a whole, the I_{ij}^T eigenvector $\hat{e}_i^{\text{tot}}(z)$ which corresponds to its larger eigenvalue, $\lambda_3(z)$ at a given redshift z , defines the direction along which the overall LV elongation has been maximum until this z . Similarly, $\hat{e}_1^{\text{tot}}(z)$ corresponds to the direction of overall minimum stretching of the LV up to a given z . It is very interesting to analyse whether or not there exists a change in such directions as cosmic evolution proceeds. In Fig. 3, we show the histograms for the quantities $A_i(z)$, the angle formed by the eigenvectors $\hat{e}_i^{\text{tot}}(z)$ and $\hat{e}_i^{\text{tot}}(z_{\text{low}})$, with $i = 1, 2, 3$, where ‘tot’ stands for the eigenvectors of the I_{ij}^T tensor corresponding to the total mass of the LV, at redshifts $z = 10, 5, 3, 1, 0.7, 0.5, 0.25, 0.1$. That is, we measure the deviations from the eigendirections at a given z with respect to the final ones⁷. We see that on average these directions are frozen at $z_{\text{froz}} \sim 0.5$, in such a way that only a few LVs change the eigenvectors of their total mass distribution at $z \leq z_{\text{froz}}$, while at $z \geq z_{\text{froz}}$ more and more LVs do it. This behaviour is illustrated by Fig. 4, where the evolution of the $A_i(t)$ for a typical LV case is plotted. We observe that $A_i(z)$ smoothly and gradually vanish before $t/t_U = 1$, this behaviour being common to all the LVs.

This is particularly interesting, because as we will see in Figs 6 and 7 the evolution of the I_{ij}^T eigenvalues (or, equivalently, that of its principal axes of inertia a, b, c), also declines before $t/t_U = 1$.

It is also important to investigate if there exists a component effect in the freezing-out of the eigendirections. With this purpose, we have compared the directions of the principal axes of inertia that arise from the whole mass distribution with the ones derived from every component at different redshifts (see Fig. 5). We have found that the latter are mainly parallel to \hat{e}_i^{tot} in the DM and cold baryon cases. Concerning hot gas, the distribution of the angles, θ_i , formed by \hat{e}_i^{tot} and $\hat{e}_i^{\text{hot bar}}$, the eigenvectors of the hot gaseous component, starts nearly uniform and as time elapses a peak around 0° arises, as we can observe in Fig. 5 for the \hat{e}_1 case.

This means that DM dynamical evolution determines the preferred directions of LV stretching, and cold gas particles closely follow them. Hot gas particles (in this case, as explained in §4, gaseous particles not trapped into singularities and heated by gravitational collapse), on the contrary, do not follow DM evolution at high redshifts, but they trace at any z the locations where mass sticking events have taken place. Indeed, as explained in §4, gas gravitational heating is due to the transformation of the ordered flow energy into internal energy at CW element formation.

6 ANISOTROPIC EVOLUTION: SHAPES

Before we focus on the statistical analysis of our results, we present the shape evolution of some selected LVs in order to show how they acquire their filamentary or wall shape. Then, we analyse the

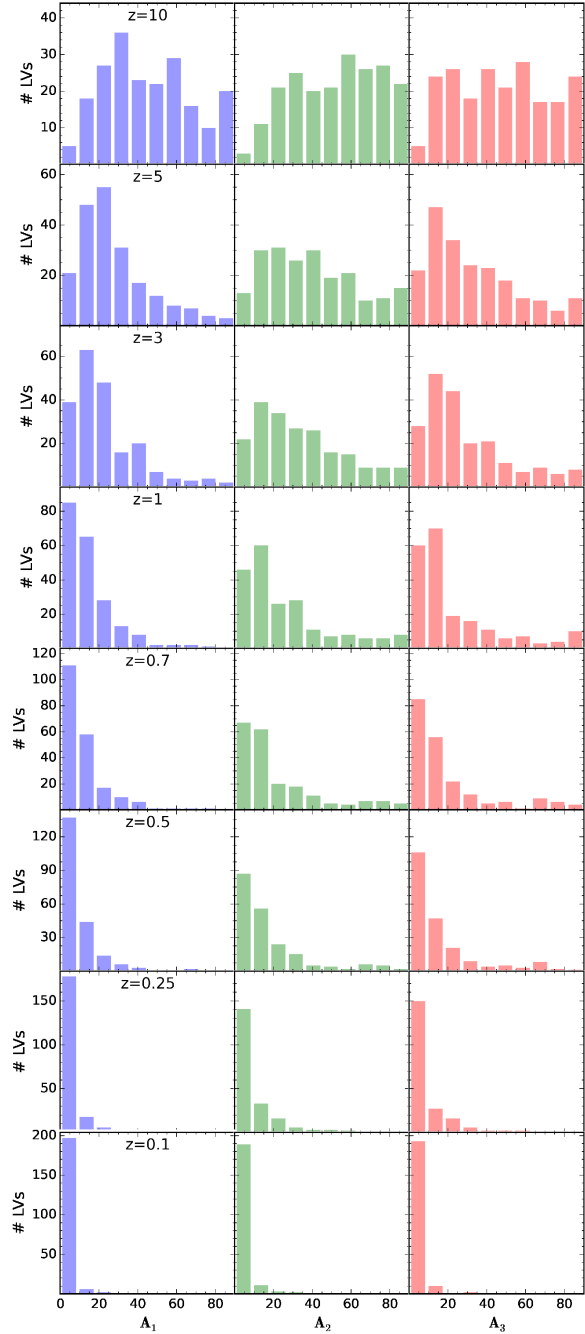


Figure 3. Evolution across redshifts of the A_i distribution, where A_i is the angle formed by the eigenvectors $\hat{e}_i^{\text{tot}}(z)$ and $\hat{e}_i^{\text{tot}}(z_{\text{low}})$, with $i = 1, 2, 3$, and where ‘tot’ stands for the eigenvectors of the I_{ij}^T , calculated with all the LV components.

⁷ Note that only two out of the three A_i angles are independent in such a way that if for instance $A_1 = 0$ then $A_2 = A_3$.

shape evolution of all the objects in our sample, by considering component as well as mass effects. To that end, LVs are grouped according to their mass, M , into three bins, massive ($M \geq 5 \times 10^{12} M_\odot$), intermediate mass ($5 \times 10^{11} \leq M < 5 \times 10^{12} M_\odot$) and low-mass LVs ($M < 5 \times 10^{11} M_\odot$).

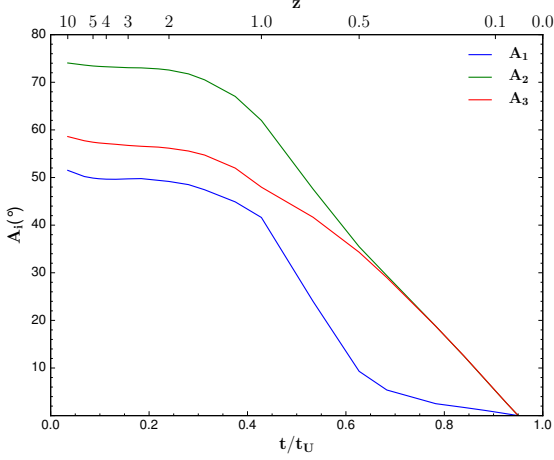


Figure 4. An example of the $A_i(t)$ evolution, where A_i is the angle formed by the eigenvectors $\hat{e}_i^{\text{tot}}(z)$ and $\hat{e}_i^{\text{tot}}(z_{\text{low}})$, with $i = 1, 2, 3$ and t is given in terms of the age of the Universe (t_U).

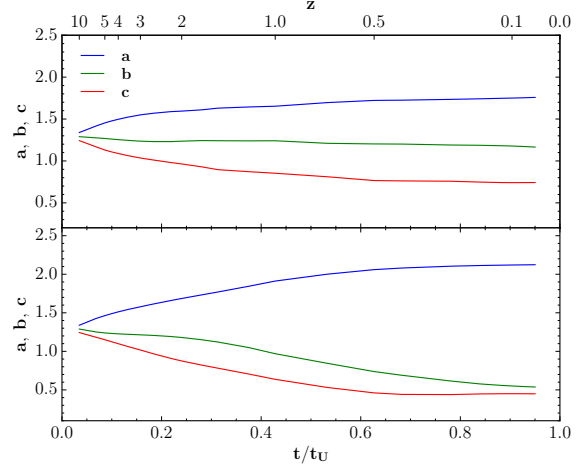


Figure 6. Evolution of the principal axes of inertia for two LVs. Top, LV on the left-hand side of Fig. 2, with a wall-like structure. Bottom, LV on the right-hand side of Fig. 2, which acquires a filamentary shape.

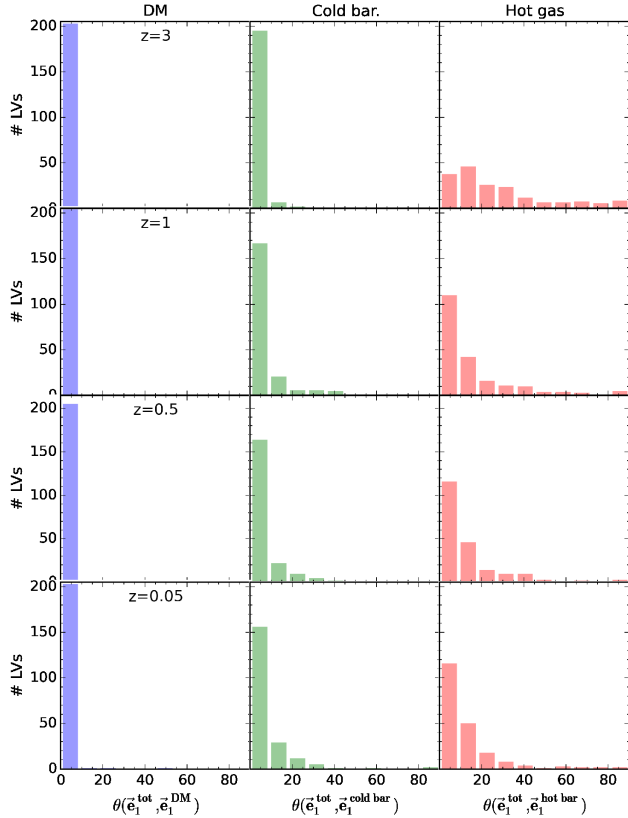


Figure 5. Distributions of the angles formed, at several redshifts, by the direction of the $\hat{e}_1^{\text{tot}}(z)$ axis of inertia that arise from the overall matter distribution with the same axis calculated with the different components.

6.1 Two particular examples of shape evolution

In Fig. 6, we exemplify the evolution of the principal axes of the inertia ellipsoid for the LVs of Fig. 2. The upper plot (LV on the left-hand side of Fig. 2) illustrates an LV that has two axes that expand across time, i.e., it has a flat structure. The lower plot corresponds to the LV on the right-hand side of Figure 2 and portrays

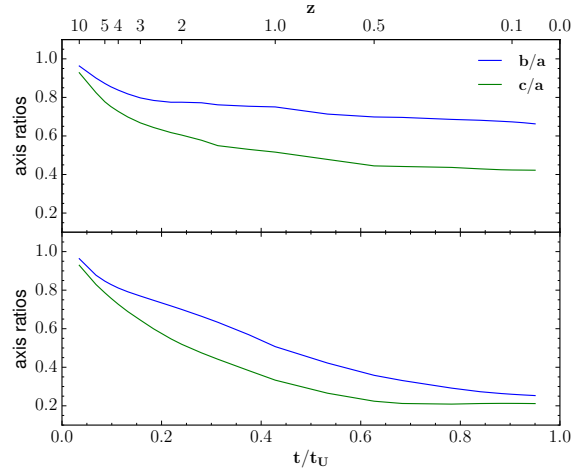


Figure 7. Axis ratio evolution of the Lagrangian volumes of Fig. 6. The upper plot shows the evolution towards an oblate shape and the lower plot shows an LV that acquires a prolate shape.

the case in which the major axis grows while the other two axes are compressed, giving in consequence a prolate shape. This result can also be inferred from Fig. 7, where we can see the evolution of the axis ratios b/a and c/a for the same LVs of Fig. 6. In the lower plot of Fig. 7, we observe that the two minor axes end up close to each other in length, therefore the LV has a filamentary structure. The upper plot, in contrast, has the minor axis significantly shorter than the other two, hence having an oblate shape.

A remarkable result is the continuity of the $a(t)$, $b(t)$ and $c(t)$ functions for all the LVs, with no mutual exchange of their respective eigendirections across evolution, i.e., the local skeleton is continuously built up, in consistency with Hidding, Shandarin & van de Weygaert (2014).

6.2 Generic trends of shape evolution

In this subsection, the generic trends of shape evolution are examined at a qualitative level. In Fig. 8, where the axis ratios are plot-

ted, we can note that the selected LVs are gathered on the nearly spherical zone ($c/a \geq 0.8$) by construction, except the hot gaseous component. As time elapses, LVs are deformed, and their evolution is shown as they move down inside the triangle described by the axes b/a , c/a and $T = 1$ (orange line). Accordingly, at $z = 0.05$ they tend to be spread over the triangle. Note that intermediate mass and low-mass objects evolve faster than the massive ones. At z_{low} , DM is preferentially located in the $T > 0.3$ and $c/a < 0.4$ region, therefore we end up with more prolate systems than oblate objects. This assertion is valid for the total, DM and cold baryons axis ratio evolution. In contrast, hot gas does not seem to show a remarkable evolution effect as it appears populating roughly the same regions of the aforementioned triangle at redshifts 10, 5 and 3, and later on, excluding either the oblate area on the right or the prolate one at the left bottom corner of the triangle.

The shape evolution of the LV mass distribution is also shown in Fig. 9, where shape distortions are represented in the prolateness-ellipticity plane. In this case, LVs move inside the triangle bound by the lines, $e = p$ (prolate spheroids), $p = -e$ (oblate spheroids) and $p = 3e - 1$ (flat objects). We observe the same pattern as in Fig. 8, for the total components, DM and cold baryons. In other words, initially spherical systems, concentrated on one corner of the triangle, evolve across redshifts filling up the triangle, so that, at $z = 0.05$, we end up with a high percentage of prolate triaxial objects, $\sim 83\%$ for the total inertia ellipsoid. We have also found that $\sim 91\%$ of the selected LVs have extreme total ellipticities ($e > 0.5$), while only 8% have moderate ones. A significant percentage of the analysed objects are extremely prolate, $\sim 31\%$, that is, they have a thin filament-like shape. At $z = 0.05$, we can find systems close to the flat limit, specially in the case of cold baryons. As in the previous figure, hot gas does not present a remarkable evolution effect after $z = 1$. At higher zs , however, the hot gas in some LVs show needle-like as well as flat shapes (see panels corresponding to $z = 5$ and, to a lesser extent, at $z = 3$), but these shapes do not appear anymore at lower zs .

Figs 8 and 9 nicely show generic trends of shape evolution. More elaborated, quantitative analyses of component and mass effects are given in the next sub-sections.

6.3 Component effects

In order to quantitatively determine if there is a component effect on the LV shape evolution (i.e., whether DM, hot and cold baryons behave dissimilarly), we represent the cumulative distribution function (CDF) of the e , p and T parameters in Figs. 10 and 11.

Each row in Fig. 10 shows the cumulative probability of the e parameter calculated for DM, cold baryons, hot gas and the total components at a given redshift. The first column depicts the result obtained for all the LVs and the other columns display our findings split according to the binning in LV mass. As we can observe, the DM and cold baryonic components move from low ellipticities or high sphericities at high redshifts towards higher ellipticities at z_{low} . As a result, these components acquire a filament-like structure (see Fig. 10). Note that cold baryons and DM exhibit approximately the same behaviour as time elapses. At z_{low} cold baryons are slightly more prolate than the DM component, specially in the case of low-mass LVs. On the other hand, the hot gaseous component does almost not experience an evolution effect, as can be noted from the ellipticity CDFs in Fig. 10, whether or not we group the LVs according to their mass. Hot gas has an $\bar{e} \sim 0.57$ since $z = 2$, and does not present any preference for either a spherical or a filamentary structure.

Similar conclusions can be extracted from the DM, cold baryon and hot gas prolateness CDFs (see first row of Fig. 11). In this case, hot gas has an \bar{p} ranging from 0.25–0.34 since $z = 2$. An important difference with respect to the ellipticity CDFs is that at z_{low} , hot gas cumulative probabilities show a small deviation from cold baryons CDFs which is bigger in the low-mass bin, while in the e case these components exhibit a large deviation from each other.

Triaxiality CDFs show a tendency of cold baryons to have a prolate shape independently of the mass binning at $z = 3$. We observe the same displacement of DM and cold baryon CDFs across redshifts, previously noted from ellipticity and prolateness cumulative probabilities. Concerning hot gas, it has an \bar{T} in the range 0.69–0.76 since $z = 2$, showing almost no changes thereafter. This displacement causes that the difference between DM, cold and hot baryons CDFs appears greatly diminished at $z = 1$. This fact can also be noticed from ellipticity and prolateness CDFs. It is noteworthy that the cold baryon triaxiality cumulative probability of the massive LV bin is delayed with respect to the DM CDF at $z = 1$. This difference is kept at $z = 0.05$ (see lower panels of Fig. 11), this is also true for the prolateness case. On the contrary, at z_{low} DM CDF appears delayed with respect to cold baryons for the low-mass bin.

6.4 Mass effects

To study the impact of the LV mass on its shape deformation, we plot in Figs 12 and 13, the CDF split by the component considered in the reduced inertia tensor calculation. From left to right we show in each column results obtained with all the particles, taking into account only DM particles, then cold baryons results and finally hot gas. Rows in Fig. 12 show cumulative probabilities at different redshifts. Each panel present the CDF calculated according to the binning in LV mass, massive object CDF are shown in magenta, intermediate mass results in cyan and low-mass CDF in blue.

In the first place, we discuss the ellipticity CDFs in Fig. 12. As we can observe, the mass effects are not very relevant and moreover they almost do not evolve. The most important mass effects appear in cold baryons at any z . Indeed, the massive and low-massive LV samples at $z = 3$ and 1 have been determined to be drawn from different populations with the two-sample Kolmogorov–Smirnov test with 90% CI; while the massive and intermediate mass LV samples with 95% CI at $z = 3, 1$ and 0.05. In general, massive LVs tend to be more spherical across redshifts, and they have a narrower e distribution than less massive ones.

In the prolateness case, the mass effects grow with time, except in the hot gaseous component. Hot gas independently on the mass binning is less spherical than the other components at $z = 3$. At $z = 1$, massive LVs are more spherical than the less massive ones for both DM and cold baryons. The mass effect is less pronounced in the case of hot gas. At z_{low} the tendency described above is kept (see upper panels in Fig. 13). The p distribution in massive LVs is narrower than those in the other mass bins and it becomes wider faster in the low-mass bin.

Regarding triaxiality CDFs, again mass effects grow with evolution, mainly in the DM component (see lower panels in Fig. 13). We can also note that in both, the total and the DM case, there are almost no systems with $T < 0.6$, specifically, there is a lack of oblate massive objects relative to the other mass groups. We have tested the difference between the massive and the low-massive bins with the two-sample Kolmogorov–Smirnov test at a 90% CI. This mass effect is less significant in the baryon case. Indeed, cold

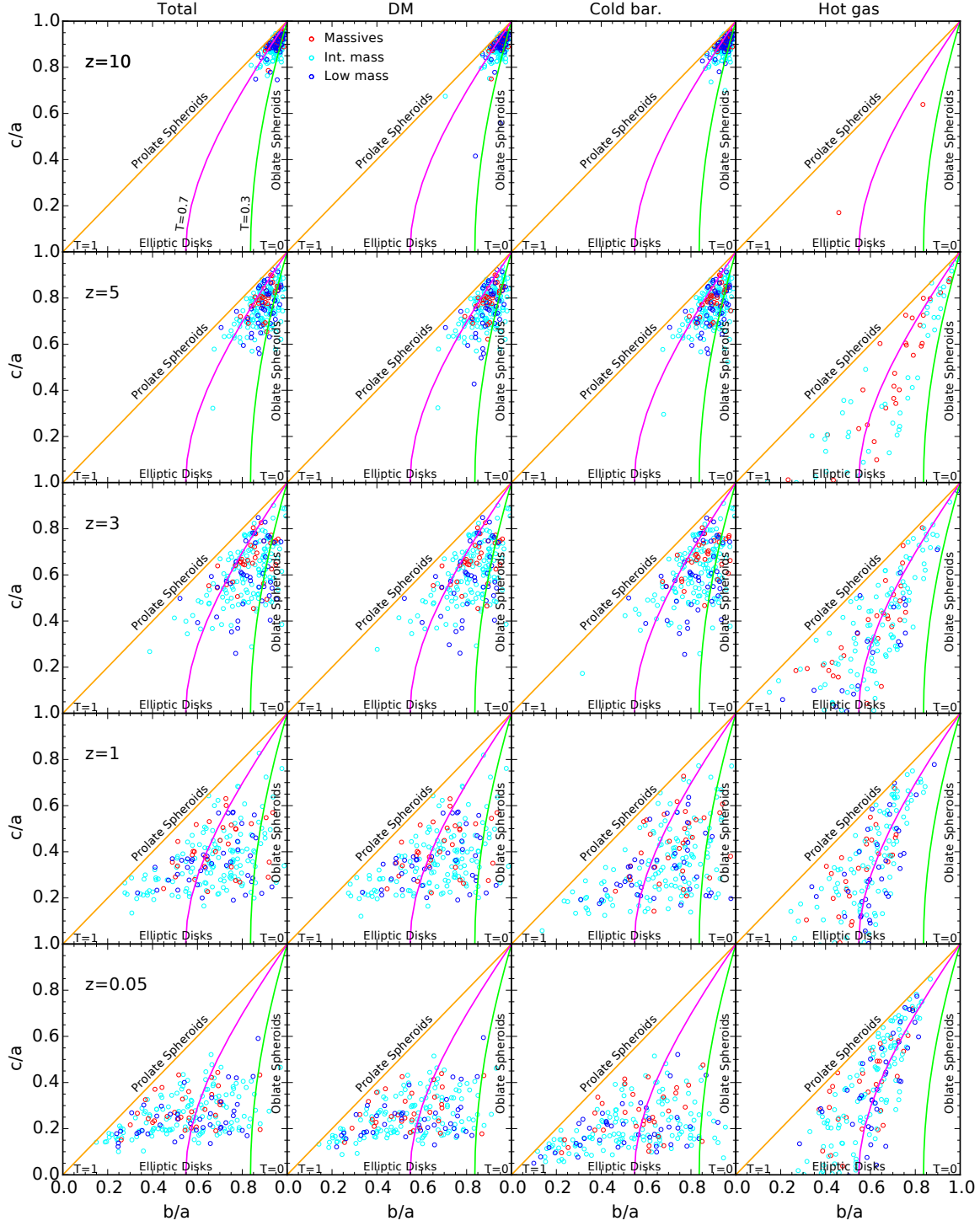


Figure 8. Axis ratio evolution of all the selected LVs, where coloured circles indicate different mass range. Massive LVs with $M \geq 5 \times 10^{12} M_{\odot}$ are represented in red, LVs with intermediate mass, $5 \times 10^{11} \leq M < 5 \times 10^{12} M_{\odot}$, in cyan and low-mass LVs, $M < 5 \times 10^{11} M_{\odot}$, in blue. The orange line correspond to $T = 1$, i.e., to a prolate spheroidal shape. Objects with $c/a < 0.9$ and $T > 0.7$ (magenta line) have a prolate triaxial shape and LVs with $c/a < 0.9$ and $T < 0.3$ (green line) are prolate triaxial ellipsoids. We show the axis ratios obtained with the total number of particles, the axis ratios of DM particles, and the axis ratios found for cold and hot baryons.

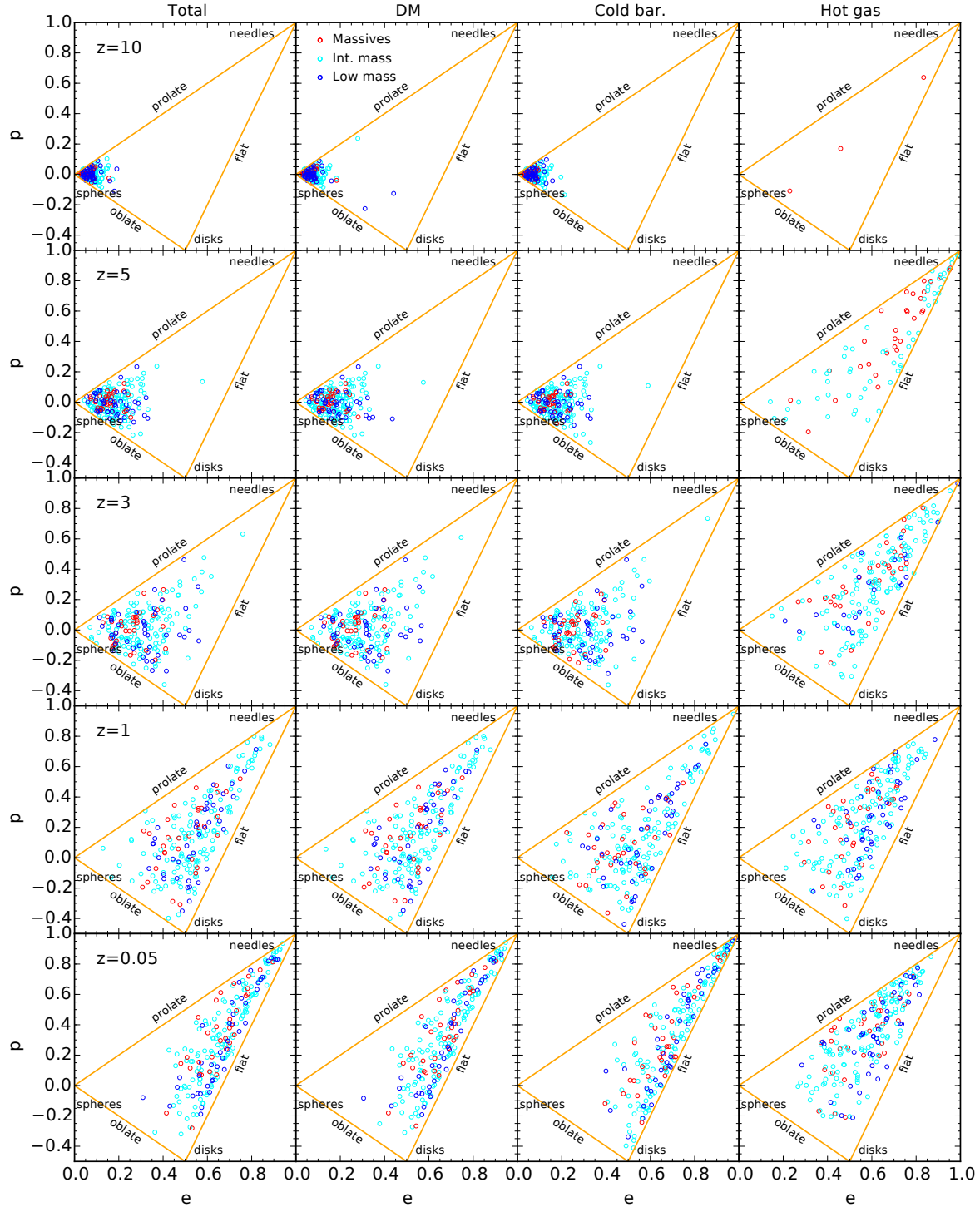


Figure 9. Prolateness-ellipticity plane for the reduced inertia tensor of the selected LVs for redshifts 10, 5, 3, 1 and 0.05. Massive LVs with $M \geq 5 \times 10^{12} M_{\odot}$ are represented in red, LVs with intermediate mass, $5 \times 10^{11} \leq M < 5 \times 10^{12} M_{\odot}$, in cyan and low-mass LVs, $M < 5 \times 10^{11} M_{\odot}$, in blue. The orange lines correspond to ultimate shapes, $e = p$ (prolate spheroids), $p = -e$ (oblate spheroids) and $p = 3e - 1$ (flat objects).

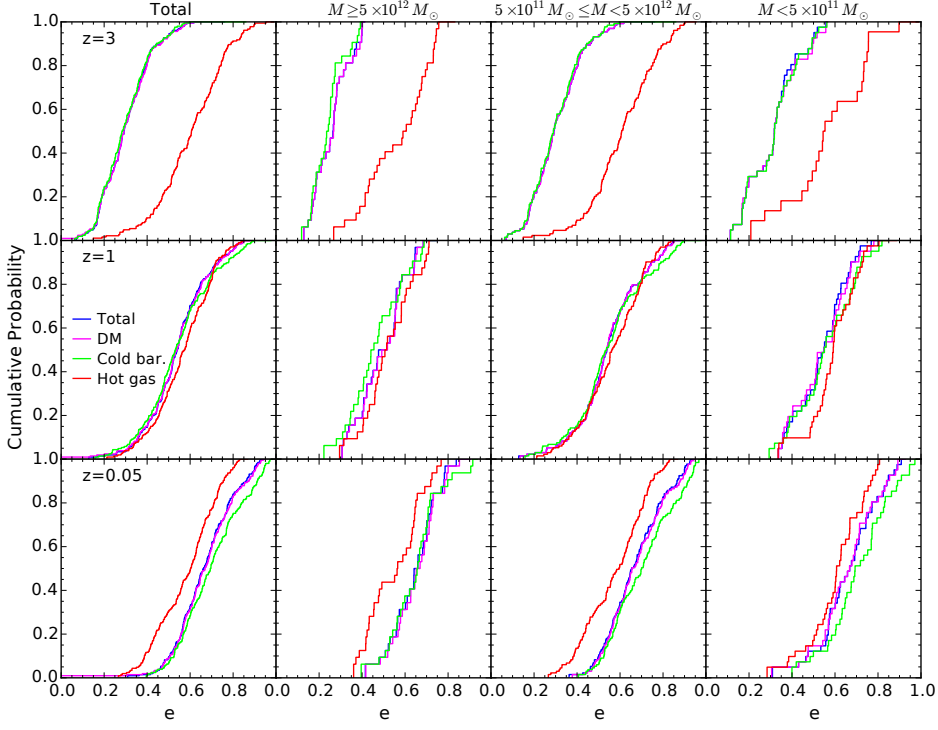


Figure 10. Cumulative distribution function of the ellipticity parameter, e , portraying component effects and their evolution in different mass bins. Each column shows the distribution binned according to the LV mass. Plots in the first column are calculated for the total number of LVs. Rows represent different redshifts. The code colour used in each plot is as follows, results obtained with the total reduced inertia tensor are presented in blue, DM results in magenta, cold baryons in green and hot gas in red.

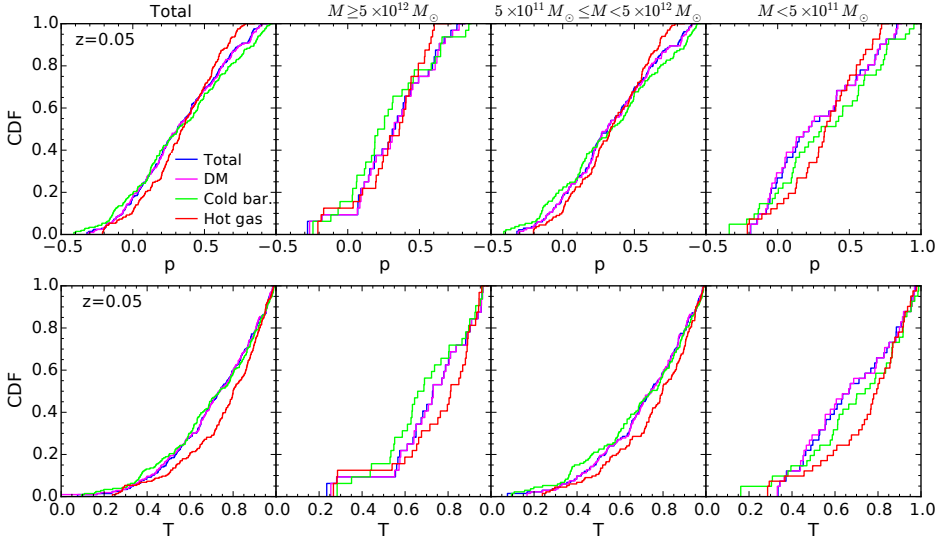


Figure 11. Upper panels, CDF of the prolateness parameter, p , at z_{low} . Lower panels, CDF of the triaxiality parameter, T , parameter at z_{low} . Each column shows the distribution binned according to the LV mass. Plots in the first column are calculated for the total number of LVs. The code colour is as in Fig. 10.

baryons do not present a significant mass effect, only less massive LVs tend to be more oblate than the more massive bins at $z = 3$ and 1.

Summing up, except for the hot gas component, more massive LVs tend to evolve slightly more slowly from their initial spherical shape than less massive ones. This can be interpreted in terms of the CW dynamics as follows: more massive objects would appear more frequently in nodes of the CW, versus less massive objects

being present in filaments and walls. Therefore, the relative importance of anisotropic mass rearrangements versus radial ones is lower in massive than in less massive LVs. Concerning the hot gas component, no relevant evolution has been detected, particularly after $z \sim 3$, indicating that neither the possible anisotropic flows towards singularities, nor the possible pressure-induced anisotropic outflows, have caused measurable LV mass rearrangements in the LV sample thereafter.

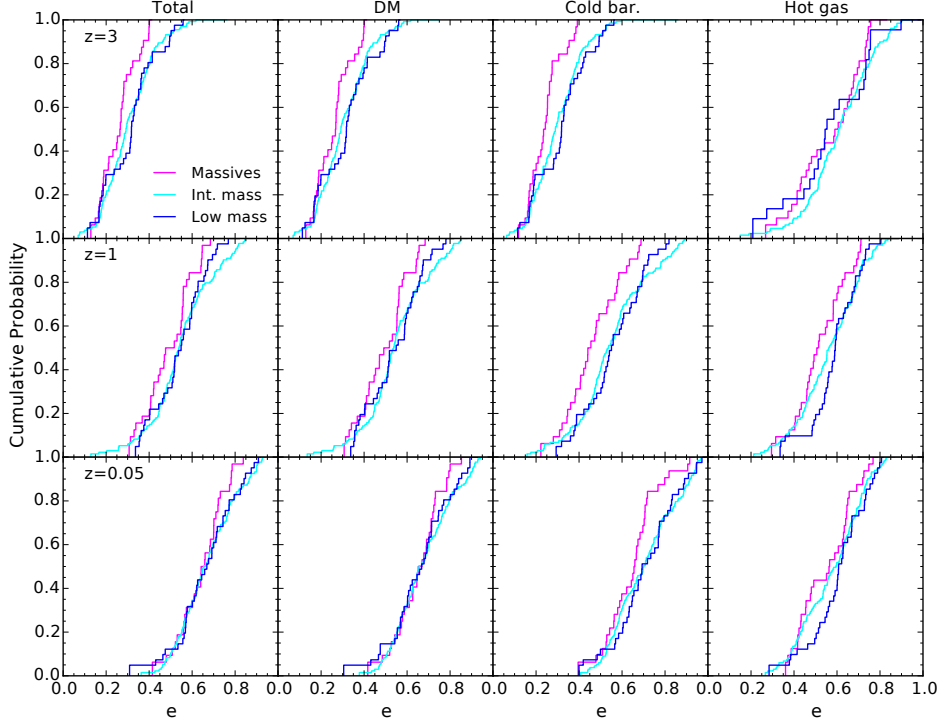


Figure 12. Cumulative distribution function of the ellipticity parameter, e , illustrating mass effects and their evolution according to the LV components. Each column displays the distribution binned according to the components taken into account to calculate the reduced inertia tensor, namely, the total number of particles, DM, cold baryons and hot gas. Rows represent different redshifts. In each plot, massive LVs ($M \geq 5 \times 10^{12} M_{\odot}$) are shown in magenta, LVs with an intermediate mass ($5 \times 10^{11} \leq M < 5 \times 10^{12} M_{\odot}$) in cyan and low-mass LVs ($M < 5 \times 10^{11} M_{\odot}$) in blue.

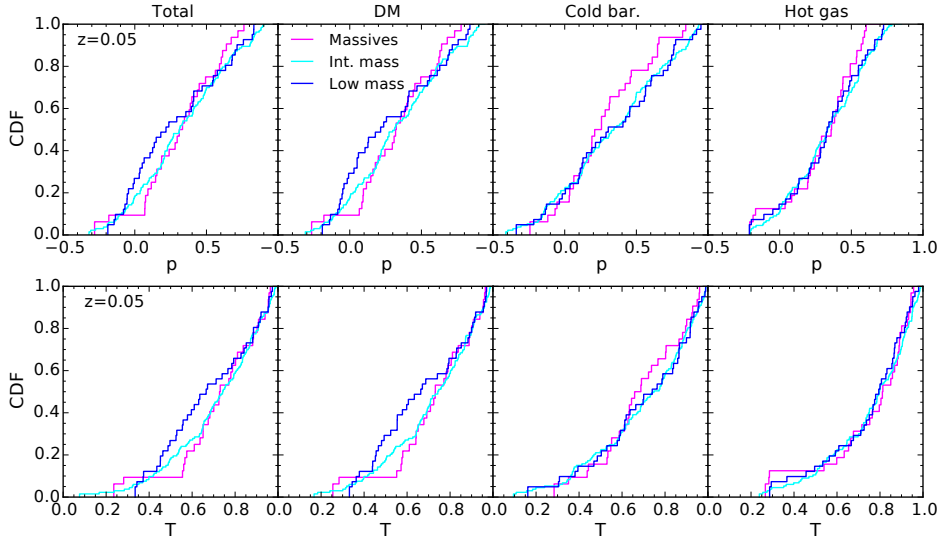


Figure 13. Upper panels, CDF of the prolateness parameter, p . Lower panels, CDF of the triaxiality parameter, T . From left to right the columns show the distribution binned according to the components taken into account to calculate the reduced inertia tensor, i.e., the total number of particles, DM, cold baryons and hot gas. The code colour in each plot is as in Fig. 12

7 FREEZING-OUT OF EIGENDIRECTIONS AND SHAPES

7.1 Freezing-out times

In the previous sections we have become aware that the $A_i(z)$, $i = 1, 2$ and 3 angles evolve with time and $\rightarrow 0^\circ$ before z_{low} . We remind that $A_i(z)$ is the angle formed by the eigenvectors $\hat{e}_i^{\text{tot}}(z)$

and $\hat{e}_i^{\text{tot}}(z_{\text{low}})$, with $i = 1, 2, 3$, where ‘tot’ stands for the eigenvectors of the I_{ij}^{r} tensor corresponding to the total mass of the LV. Also, the evolution of the LV inertia ellipsoid declines in the same limit, see Figs 4 and 6. In this section, we use the times when these eigendirections and inertia axes become frozen. We have calculated these freezing times to study and compare both processes and to look for possible mass effects. The subject is interesting to

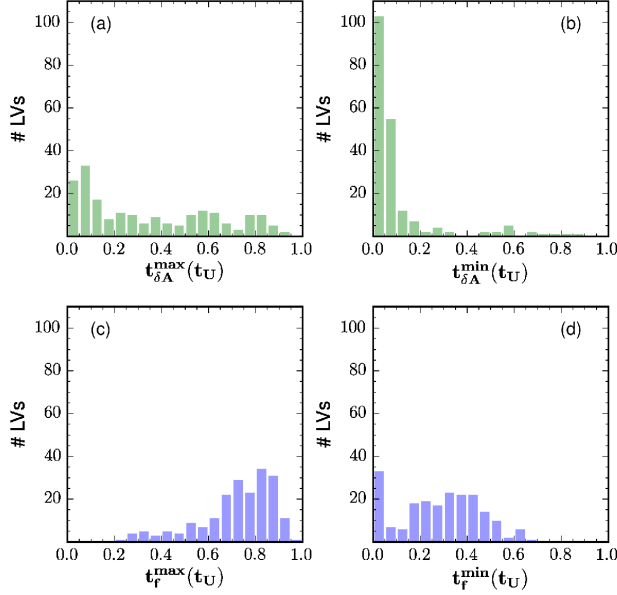


Figure 14. Histograms for $t_{\delta A}^{\max}$, $t_{\delta A}^{\min}$, t_f^{\max} and t_f^{\min} defined with $\cos(\delta A_i) = 0.9$ and $f = 0.1$.

elucidate how and when the local CW around galaxies-to-be becomes frozen at the scales analysed in this paper, while it still feeds the protogalaxies at smaller scales.

Having the $A_i(z)$ angles $\sim 0^\circ$ during a z range $z \geq z_{\text{low}}$ means that the LV deformations become fixed in their eigendirections before z_{low} , or, in other words, mass rearrangements are thereafter organised in terms of frozen symmetry axes making the inertia tensor diagonal, i.e., in terms of a skeleton-like structure. This motivates the search for the moment when a given LV gets its structure frozen. This is not a straightforward issue, however, because this situation is gradually reached: all we can do is to resort to thresholds.

In the following, we use time instead of z in order to make our results clearer. Given a threshold angle δA_i , we define $t_{\delta A_i}$ as the time (Universe age at the event in units of the current Universe age t_U) when $A_i(t) \leq \delta A_i$ if $t \geq t_{\delta A_i}$, (i.e., the Universe age when the i th eigendirection of the inertia tensor becomes fixed within an angle δA_i). Then, we define $t_{\delta A_i}^{\max}$ and $t_{\delta A_i}^{\min}$ as the maximum and minimum values of $t_{\delta A_i}$, $i = 1, 2, 3$, for each LV. That is, $t_{\delta A_i}^{\max}$ for a given LV is the fractional time when the directions of its *three* eigen vectors become frozen, or, symbolically, $A_i(t) \leq \delta A_i$ if $t \geq t_{\delta A_i}^{\max}$ for any direction⁸. The minimum $t_{\delta A_i}^{\min}$ satisfies the same condition for just one direction. Fig. 14 (upper plots) shows the distribution of $t_{\delta A_i}^{\max}$ and $t_{\delta A_i}^{\min}$ for our sample of 206 LVs with δA_i such that $\cos(\delta A_i) = 0.9$.

A very interesting point is to explore LV shape transformations relative to the freeze-out times for inertia eigendirections. An illustration can be found in Figs 4 and 6. Comparing both figures, we see that the principal axes change slightly after skeleton emergence for the particular LVs considered in this figure by using a 10% threshold (see below). The differences are larger for other LVs, and, indeed it is worth analysing this issue in more detail.

⁸ Note that the second and the third eigendirections become frozen at the same time.

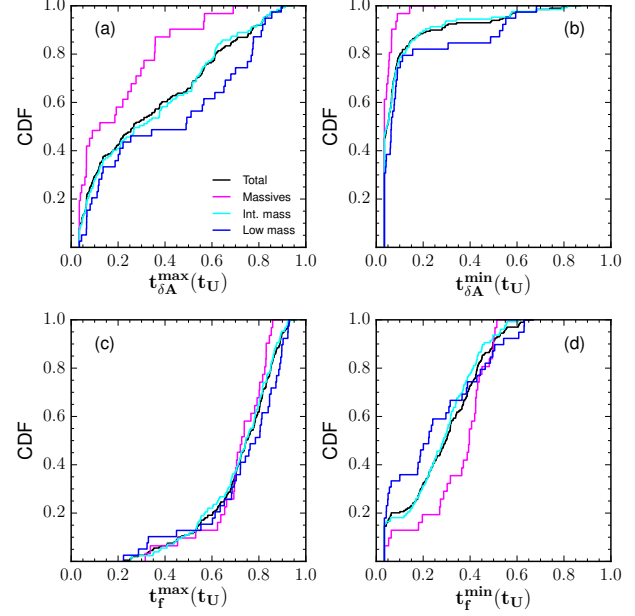


Figure 15. CDFs for the same quantities in the previous figure, showing possible mass effects.

Therefore, to be more quantitative, we define $t_{f,a}$ as the fractional time when the inertia axis a becomes frozen within a threshold f_a , which is a fixed fraction of the $a(t)$ value, i.e. $\Delta a(t) \leq f_a$ if $t \geq t_{f,a}$, where $\Delta a(t) \equiv \frac{|a(t) - a(t_{\text{low}})|}{a(t_{\text{low}})}$. Similarly, we define $t_{f,b}$ and $t_{f,c}$, and then t_f^{\max} and t_f^{\min} . The former is the time when the three inertia axes become frozen, while the latter is the time when just one axis gets frozen⁹. To have an insight of the statistical behaviour of these times, in Fig. 14 (lower plots) the histograms for t_f^{\max} and t_f^{\min} are represented for $f = 0.1$. In this figure, right-(left-)panels correspond to the times when one (three) out of the eigenvectors or the principal inertia axes become fixed within a 10% of their final values.

An interesting result is that the time range for t_f^{\max} is narrow and late. The range of $t_{\delta A_i}^{\max}$ is much wider, which means that a high fraction of LVs get at high z their three eigendirections fixed before the evolution of their inertia axes ends up. During this early time interval, LVs change their shape with frozen symmetry axes, i.e., anisotropic matter inflows onto CW elements. Another result is the t_f^{\min} accumulation at the first bin of the evolution time: these are the systems having a principal axis of inertia that keeps within a 10% of its initial value along the evolution. They are less prolate than other systems. An even higher fraction of LVs have one of their eigendirections fixed in the first 5% of the evolution time (see Fig. 14.b).

A high fraction of systems also got one frozen eigendirection, while none of their principal inertia axes is fixed yet. However, at the end of the evolution this effect vanishes (compare Figs 14.b and 14.d). Finally, let us mention that LVs also spend an important fraction of their lives with one but not three fixed eigendirections (within the thresholds used to draw these figures, compare Figs 14.a and 14.b), or one but not three frozen inertia axes (compare Figs 14.c and 14.d).

⁹ Again, once the value of one principal axis becomes fixed, the freezing times for the other two axes are the same.

7.2 Mass effects

Next, we look for mass effects in the distributions of $t_{\delta A}^{\max}$ and $t_{\delta A}^{\min}$, as well as in those of t_f^{\max} and t_f^{\min} . This is more clearly visualised in terms of cumulative histograms. In Fig. 15, we plot the CDF for $t_{\delta A}^{\max}$ and $t_{\delta A}^{\min}$ (i.e., LV eigen directions relative to their final values, first row) and t_f^{\max} and t_f^{\min} (principal inertia axes, second row), respectively, where no binning has been used. To analyse possible mass effects, results for the three mass groups are shown in each panel. The cumulative histograms in the four panels of this figure are in one-to-one correspondence with the histograms in Fig. 14.

The first outstanding result is that the time range for t_f^{\max} is roughly the same (narrow and late), irrespectively of the mass range used (Fig. 15.c). This behaviour can be understood as the consequence of $\frac{dD_+(t)}{dt} \rightarrow 0$ at late times, a global effect causing anisotropic flows to vanish, see §3.4 for more details. Nevertheless, there exists a mass effect in $t_{\delta A}^{\max}$ (Fig. 15.a), with the least-massive LVs showing a delay in the spine emergence or in getting their three eigendirections frozen with respect to more massive ones, the differences being more marked at early times. This is somewhat expected from the previous discussion on the effects of the eigenvalue landscape heights on the timing of spine emergence, in §3.4.

Fig. 15.b exhibits strong mass effects too. Indeed, at early times the most massive systems get one out of their three eigendirections frozen sooner than less massive ones. In fact, $\sim 95\%$ of the massive LV subsample has one of their eigendirections fixed at $t/t_U \simeq 0.1$. This mass segregation can be understood in the light of the considerations made in §3.4, where we concluded that the first CW elements tend to appear and percolate earlier on within massive LVs than within less massive ones.

On the other hand, the freezing-out times for the principal axis of inertia (panel 15.d) display a remarkable mass effect, although just at early times. Later on, irrespectively of their mass, no LV gets its first principal axis of inertia fixed later than $t/t_U \simeq 0.55$. This upper bound on t_f^{\min} might be a consequence of both, the $\frac{dD_+(t)}{dt} \rightarrow 0$ after the Λ term dominates the Universe expansion, and the fact that flows towards walls are the first to vanish at a local level. The mass effect lies in massive systems having their t_f^{\min} delayed at early times in relation to less massive ones (consistently with what was found in § 6.2), the difference vanishing at $z \sim 1$.

Finally, to look for correlations, the t_f^{\max} and t_f^{\min} for our sample of LVs are plotted versus their respective $t_{\delta A}^{\max}$ and $t_{\delta A}^{\min}$, in Fig. 16 for $f = 0.1$ and $\cos(\delta A_i) = 0.9$. No outstanding correlation exists in any case, but we see that indeed, most systems have their eigendirections fixed before their principal axes got frozen.

Summing up, we observe that on average eigendirections (either one or the three) for massive LVs become fixed at earlier stages than that of less massive LVs. Nevertheless, no relevant mass effects are found for principal inertia axis freezing times. In addition, eigendirections become in general fixed before mass flows onto the corresponding CW elements stops, the time delay being particularly long for the first eigendirection relative to the first principal axis in massive systems. Thus, the first eigendirection in massive systems gets fixed quite a while before the accretion onto it stops.

8 DISCUSSION: POSSIBLE SCALE EFFECTS

In Section 2.2, when describing how to build up the LV sample, a value of $R_{\text{high}} = K \times r_{\text{vir,low}}$ with $K = 10$ has been chosen to define the LV at z_{high} . As explained there, this choice was motivated as a compromise between low K values, ensuring a higher number

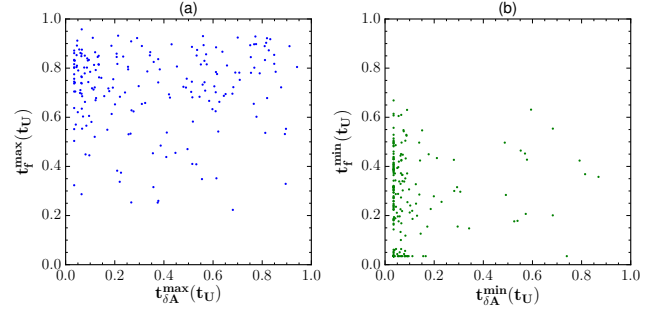


Figure 16. Scatter plots of t_f^{\max} versus $t_{\delta A}^{\max}$ (left) and t_f^{\min} versus $t_{\delta A}^{\min}$ (right).

of LVs in the sample, and a high K , ensuring LVs with high enough number of particles so that we obtain meaningful LVs. However, $K = 10$ is by no means the unique value that satisfies these constraints. Therefore, it is important to test out the possible effects of changing this value under the same constraints.

To this aim, we have repeated all the calculation using $K = 7.5$ and 15 . The LV building up (see section 2.2) has been repeated with the same SKID identified haloes at z_{low} as first step. Nonetheless, when $K = 15$ is used, some of the LVs do not satisfy anymore the condition of having all their particles inside the hydrodynamic zoomed volume. These particular LVs have been removed from the initial sample of 206 LVs, in such a way that we are finally left with 159 LVs for $K = 15$. This problem does not exist when using $K = 7.5$; however, to probe the scale effects, we need samples that contain the same z_{low} SKID-identified haloes as starting point in the three scales. Therefore, only these 159 well-behaved LVs (a subset of the initial $K = 10$ sample) have been used to analyse the scale effects.

The first relevant outcome is that there is no substantial difference when results obtained with the subsample of 159 LVs and with the sample used along this paper (206 LVs) for $K = 10$ are compared.

In the following subsections, we will compare the results obtained with each of the three samples of 159 LVs, dubbed according to its K value, $K_{7.5}$, K_{10} and K_{15} .

8.1 Effects on eigenvector orientation evolution

Concerning the evolution across redshifts of the I_{ij}^T eigendirections relative to their final values at z_{low} (Fig. 3), no relevant differences have been found between the histograms obtained with the K_{15} and K_{10} samples at the same redshifts. Fig. 17 illustrates this behaviour, showing that the A_1 angle distributions for K_{15} are similar to those found with K_{10} at different z pairs, see §8.3 for more details.

In addition, no scale effects appear in the angles formed by the eigenvectors, $\hat{e}_i^{\text{tot}}(z)$, $i = 1, 2, 3$, arising from the overall matter distribution with the same eigenvectors calculated with the different components (i.e., those angles whose distribution for the sample of 206 objects is given in Fig. 5.)

8.2 Effects on shape evolution

To gain further insight, the 159 LV subsample has been split according to the LV masses. In order to assure that we are comparing the same mass bins for the three scales, we have mapped the LVs

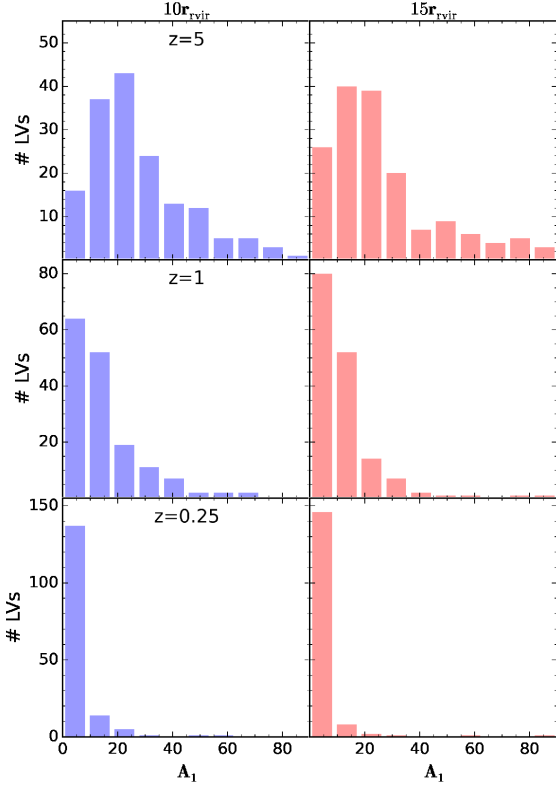


Figure 17. Histograms of the A_1 distribution at different redshifts for the K_{10} and K_{15} samples (left- and right-hand columns, respectively).

belonging to the three mass ranges defined for the K_{10} sample to the LVs of the K_{15} and $K_{7.5}$ scales.

Important results concerning shape evolution are as follows.

(i) No relevant differences in the evolution patterns have been found between the least massive LV group ($M < 5 \times 10^{11} M_\odot$ in the K_{10} sample) when followed in the K_{15} , K_{10} and $K_{7.5}$ samples (see Fig. 18, blue lines). That is, these LVs are hardly sensitive to the K scale in their evolution. The scale effects are only slight between the K_{15} and K_{10} samples when no mass splitting in the LV sample is performed (see Fig. 18, black lines).

(ii) LVs in the massive group are sensitive to the K scale, with the $K_{7.5}$ samples showing particular differences. Fig. 18 is an example of such a behaviour, likely due to the wall effect, whose formation is better sampled with K_{15} . Also, walls are more frequent in massive LVs. See §8.3 for more details.

(iii) In any case, the qualitative results reached in § 6 about component effects in shape deformations are stable when comparing K_{15} and K_{10} samples.

8.3 Effects on freezing-out times

Fig. 19 shows the histograms for the $t_{\delta A}^{\max}$, t_f^{\max} , $t_{\delta A}^{\min}$, and t_f^{\min} times for samples using different K scales. It is clear from this figure that while the results for the K_{15} and K_{10} samples are roughly consistent with each other, those for the $K_{7.5}$ sample differ. The only exception is the t_f^{\max} time distribution (second row), whose pattern is the same at any scale, namely rather late and peaked. Recall that t_f^{\max} is the time when the three inertia axes are fixed to within 10% of their final values, i.e., the time when all anisotropic

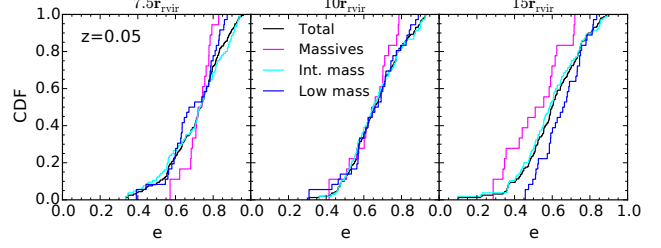


Figure 18. CDFs of the ellipticity at z_{low} portraying mass effects obtained with the three different scales, $K_{7.5}$, K_{10} and K_{15} .

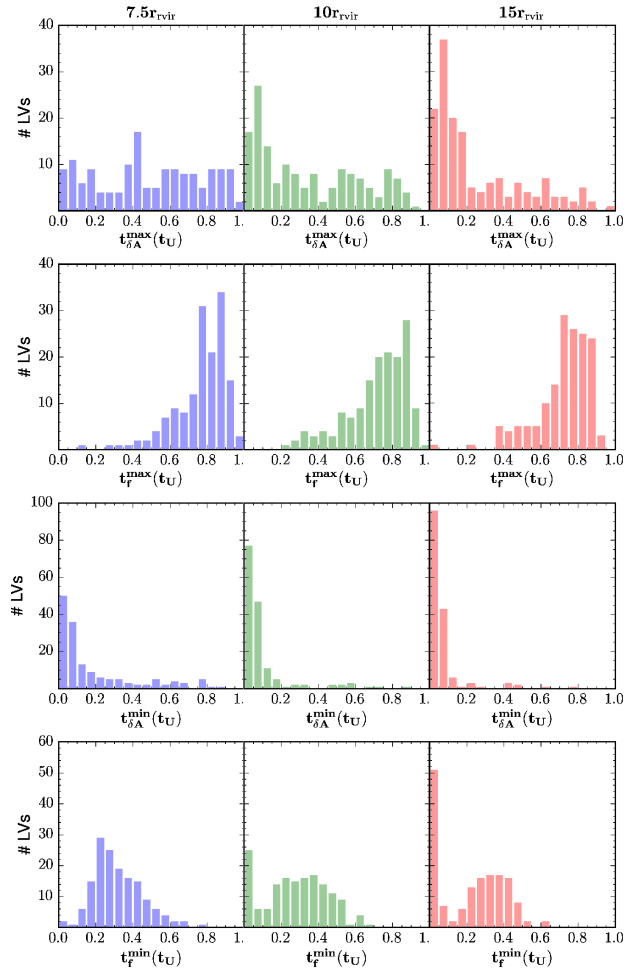


Figure 19. Histograms for $t_{\delta A}^{\max}$, $t_{\delta A}^{\min}$, t_f^{\max} and t_f^{\min} defined with $\cos(\delta A_i) = 0.9$ and $f = 0.1$. Columns show the results obtained for the three samples, $K_{7.5}$, K_{10} and K_{15} .

fluxes stop. This behaviour can be understood as the consequence of $\frac{dD_+(t)}{dt} \rightarrow 0$ at late times, that is a global effect.

A key point to understand some aspects of Fig. 19 behaviour, is the fact that the $K_{7.5}$ scale is too short to suitably sample the whole process of wall formation within some LVs. As a consequence, since the first flows to vanish are those towards walls (see § 3.4), the t_f^{\min} time (when the first inertia axis is fixed to within 10% of its final value) will be delayed at high z in the $K_{7.5}$ sample, as observed in Fig. 19, fourth row. A remarkable result is that, irrespective of the K scale, no LV has its first inertia axis frozen later

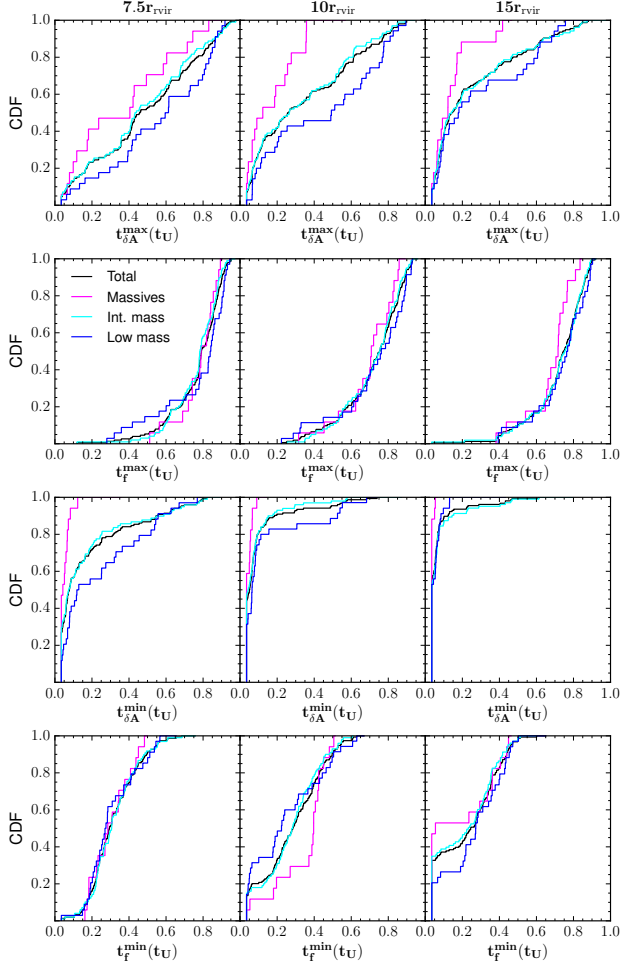


Figure 20. CDFs of $t_{\delta A}^{\max}$, $t_{\delta A}^{\min}$, t_f^{\max} and t_f^{\min} at different K scales.

than $t/t_U \simeq 0.55$. This result reinforces our interpretation given in § 7.2 that this effect is, at least partially, a consequence of the $\frac{dD_+(t)}{dt} \rightarrow 0$ tendency at latter times.

The process of wall formation could be also the reason of the similarities and differences found in the distributions of the $t_{\delta A}^{\min}$ times (when the first eigenvector direction is fixed to within a 10%). The panels of the third row of Fig. 19 show that their distributions are always peaked towards very early times, meaning that the \hat{e}_3 eigenvector of the I_{ij}^T for some LVs freezes its direction very early, following wall formation. In addition, we see that as we move from K_{15} to K_{10} to $K_{7.5}$, a delay appears, not so relevant between the K_{15} and K_{10} samples. Again, this can be interpreted in terms of the inadequacy of the shorter scale to properly catch the characteristics of wall formation in some LVs.

Finally, we address the scale effects on $t_{\delta A}^{\max}$ (first row of Fig. 19). These are the times when the LV orientations become frozen to within 10% of their final values, i.e., the times marking the skeleton emergence locally within each LV. While its distribution is rather peaked at early times for both, the K_{15} and the K_{10} samples, it flattens as we go to $K_{7.5}$. Once again, the poor wall formation sampling in most $K_{7.5}$ LVs is likely to be the cause of this difference.

It is worth noting that the qualitative features found in § 7 are stable under the change in K . For instance, mass effects can be analysed from Fig. 20, where we show the $t_{\delta A}^{\max}$, t_f^{\max} , $t_{\delta A}^{\min}$ and

t_f^{\min} mass-binned CDFs (first, second, third and fourth rows, respectively), at different scales (columns). Then, we can note that, regardless of the K value, the $t_{\delta A}^{\max}$ and $t_{\delta A}^{\min}$ distributions show qualitatively similar mass effects, with the most massive LV group fixing either one or their three eigenvalues earlier on than LVs in the intermediate or less massive group (as expected). Moreover, the t_f^{\max} distribution does not show relevant mass effects whatever the considered scale. Finally, irrespective of the scale, the t_f^{\min} distributions do not show relevant mass effects after $t/t_U \simeq 0.4$, as expected from the previous analyses. At low z , some mass segregation is found, and furthermore, it qualitatively depends on the scale. This is the only one exception to the stability under the change in K . These results could reflect the difficulty of catching the end of the mass flows in only one direction when the contribution of wall formation is combined with mass effects.

Summing up, the differences in the freezing-out times are not very relevant when using the K_{15} or the K_{10} samples. Their distributions show similar patterns, in particular when mass effects are considered.

9 SUMMARY AND CONCLUSIONS

In this paper, we present a detailed analysis of the local evolution of 206 Lagrangian Volumes (LVs) selected at high redshift around proto-galaxies. These galaxies have been identified at $z_{\text{low}} = 0.05$ in a large-volume hydrodynamical simulation run in a Λ CDM cosmological context and they have a mass range $1 - 1500 \times 10^{10} M_{\odot}$. We follow the dynamical evolution of the density field inside these initially spherical LVs from $z_{\text{high}} = 10$ up to $z_{\text{low}} = 0.05$, witnessing mass rearrangements within them, leading to the emergence of a highly anisotropic, complex, hierarchical organisation, i.e., the *local* cosmic web (CW). Indeed, at z_{low} LVs acquire overall anisotropic shapes as a consequence of mass inflows onto singularities along cosmic evolution, in such a way that some relevant aspects of these mass arrangements can be described in terms of the reduced inertia tensor I_{ij}^T evolution, as given by its principal directions and inertia axes, $a \geq b \geq c$.

Our analysis focuses on the evolution of the principal axes of inertia and their corresponding eigendirections, paying particular attention to the times when the evolution of these two structural elements declines. In addition, mass and component effects (either DM, cold or hot baryons) along this process have also been investigated.

In broad terms, we have found that local LV evolution follows the predictions of the Zeldovich Approximation (ZA, Zel'dovich 1970) and the Adhesion Model (AM, Gurbatov & Saichev 1984; Gurbatov, Saichev & Shandarin 1989; Shandarin & Zeldovich 1989; Gurbatov, Malakhov & Saichev 1992; Vergassola et al. 1994) when both caustic dressing (Domínguez 2000) and mutual gas versus CW effects (see Section 3 and Domínguez-Tenreiro et al. 2011; Metuki et al. 2015) are taken into account. Evolution also entails baryon transformation into stars inside the densest regions of the web and gravitational gas heating following the collapse. More specifically, these are our main results.

Dark matter dominates dynamically the LV shape deformations over the baryonic component, as expected from hierarchical structure formation. Deformations transform most of the initially spherical LVs into prolate shapes, i.e. filamentary structures, in good agreement with previous findings (Aragón-Calvo, van de Weygaert & Jones 2010; Cautun et al. 2014). Cold baryons follow DM behaviour in general, but with some departures from it, de-

partures that rise as evolution proceeds. Accordingly, the number of LVs having their cold baryonic principal axes in directions that differ from the ones calculated with their DM content is negligible at z_{high} , and it keeps low along the evolution, but increases with time ($\sim 25\%$ at z_{low}). On the contrary, the hot gas eigendirections have a flatter distribution at z_{high} and then they tend to converge to those calculated with DM. However, only \sim half of them reach such convergence at z_{low} . This tendency towards convergence is due to the fact that the hot gaseous component traces the locations where sticking events, in particular filament and node formation, have taken place. The mass fraction involved in these processes increases with evolution, and consequently we expect a tendency of the hot gas to be aligned with the total eigendirections.

In terms of shape evolution, a clear component effect has been found regarding the way how the evolution occurs. In fact, hot gas shapes do not exhibit important evolution because, as said above, gravitationally heated gas marks out the places where sticking events have taken place, and because, in addition, no evidence for important anisotropic mass rearrangements in this component have been found in this paper. The only remarkable effect is that the needle-like or flat shapes shown by hot gas in some LVs around $z = 5$, are transformed at lower z s. As mentioned before, DM and cold baryons shapes do evolve, with cold baryons achieving an even more pronounced filamentary structure than DM ones as a consequence of dissipation. Additionally, some mass effects have also been found in the generic evolution of shapes, with lower mass LVs evolving towards more pronounced filamentary structures on average and earlier on than the more massive ones.

A remarkable result of our analyses is that the evolution of LV deformations declines. This means that both the LV eigendirections, as well as their principal axes of inertia (a , b and c) values become roughly constant before z_{low} . This is a smooth effect that can be only defined in terms of thresholds. Taking a 10% of the final values, shape (i.e., a , b and c values) freezing-out time distribution has a narrow peak (~ 0.2 at each side) around $t/t_U = 0.8$. This happens later than the freezing-out times for the three LV eigendirections, whose distribution peaks around $t/t_U = 0.1$ and then it is flat until $t/t_U \sim 0.8$ when it decays.

By plotting individual freezing times for shapes and eigendirections, respectively (see Fig. 16.a), we note that first, most of the LVs fix their three axes of symmetry (like a skeleton), and later on their shapes are fixed. This result is in good agreement with van Haarlem & van de Weygaert (1993); van de Weygaert & Bond (2008); Cautun et al. (2014) and Hidding, Shandarin & van de Weygaert (2014) findings. Moreover, the ZA and the AM predict that walls, filaments and nodes undergo mass flows from underdense regions to denser environments, that continue after skeleton emergence.

As a general consideration, it has been found that mass rearrangements at the scales taken into account have always been highly anisotropic. Therefore, the mass streaming towards walls and filaments has been extremely anisotropic, and, to a lesser extent, towards nodes as well. In particular, galaxy systems form in environments that have a rigid spine at scales of a few Mpc, from whose skeleton a high fraction of mass elements that feed proto-galaxies are collected.

Due to anisotropic mass accretion, it turns out that in general the direction of just *one* of the LV eigen vectors or the value of *one* of their axes get frozen while the other two still continue changing. Again, for each LV there is a time delay between the moment when the first of its eigendirections get fixed (happening within the first 20% of the Universe age) and the moment when the value of one of

its principal axes becomes constant (peaking around $t/t_U = 0.35$). Therefore, we again find a situation where first the flow direction is fixed (as a first piece in the skeleton emergence) while the mass flows persist.

Even more interesting because of its possible astrophysical implications (see discussion below) is our finding that more massive LVs fix their skeleton earlier on than less massive ones, either considering just one or the three eigendirections. These results are not surprising since the dynamical processes involved in the spine emergence are faster around massive potential wells.

Concerning shape transformation decline, there are no relevant mass effects as far as the complete shape freezing-out is considered. When just one axis value is taken into account, however, an early delay of more massive LVs compared to less massive ones clearly stands out, delay that vanishes at half of the Universe age.

When building up the LV sample at z_{high} a value of $R_{\text{high}} = K \times r_{\text{vir,low}}$ with $K = 10$ has been used to define the LV at this redshift. This choice was motivated as a compromise between low K values, ensuring a higher number of LVs in the sample, and a high K , ensuring that LVs are large enough to meaningfully sample the CW emergence around forming galaxies. As this $K = 10$ value is not the unique value satisfying these constraints, the complete analysis has been repeated using $K = 7.5$ and 15 instead. We have found that when using the $K = 15$ or the $K = 10$ samples, no relevant differences in the LV eigenvector orientations, shape deformations and freezing-out times appear. Therefore, using $K = 10$ is in a sense the best choice.

It is important to remark that no explicit feedback has been implemented in the simulations analysed here, but SF regulation through the values of the SFR parameters. We remark that the issues discussed in this paper entail considerably larger characteristic scales than the ones related to stellar feedback. Hence, it is unlikely that the details of the star formation rate, and those of stellar feedback in particular, could substantially alter the conclusions of this paper, at least at a qualitative level. Concerning the inner halo scale, we recall that to properly explore the impact of SNe feedback into filamentary patterns, high enough resolution in order to resolve SNe remnants into the Taylor–Sedov phase are needed. Such simulations are available (the NUT simulations, at sub-parsec scale), but only up to $z = 9$ (Powell, Slyz & Devriendt 2011). Therefore, we still have to wait to properly understand how SNe feedback can possibly affect the CW emergence and dynamics. However, the findings so far, at high z , suggest that the filamentary patterns are essentially untouched by SNe feedback (Powell et al. 2013).

9.1 Astrophysical Implications

The results summarised so far could have important implications in our understanding of galaxy mass assembly, raising different interesting issues.

According to our results, it takes longer for less massive systems to fix their spine, possibly making it easier for these systems to acquire angular momentum through filament transverse motions relative to the galaxy haloes. In fact, recent studies on galaxy formation (Kimm et al. 2011; Pichon et al. 2011; Tillson et al. 2015; Dubois et al. 2014) in the CW context, underline the role that filament motions in the protogalaxy environment could have had in endowing filaments, and eventually the adult galaxy, with angular momentum. If real, this effect could contribute to the mass-morphology correlation (see for instance Kauffmann et al. 2003).

Our results also point towards (major) mergers events having a high probability to occur within filaments. This is an important is-

sue, though beyond the scope of this paper. In fact, if confirmed, this could decrease the allowed merger orbital parameter values (see for example, Lotz et al. 2010; Barnes 2011), as most mergers would have these parameters constrained within the filament.

Another issue concerns the use of close pairs in merger rate calculations from observational data, under the hypothesis that these systems are bound and about to merge (see, for instance Patton et al. 2000; Bell et al. 2006; Kartaltepe et al. 2007; Patton & Atfield 2008; Robaina et al. 2010; Tasca et al. 2014; López-Sanjuan et al. 2015). In this respect, some interesting efforts have been made to correct the statistics of pairs that are close in angular distance from chance superposition effects on the line of sight, (see e.g., Kitzbichler & White 2008; Patton & Atfield 2008), whose results are used by other authors in this field. Our results reinforce the need for these analyses, in the sense that a detailed determination of these corrections, including their dependence on the galaxy properties, merger parameters and environment, could be crucial for a more elaborated understanding of the relationship among close pair statistics and merger rates.

Finally we very briefly address the question of the warm-hot gas distribution at intermediate scales. Our results point to the web structure being marked out by hot gas from high redshifts. Indeed, at scales of 4 – 8 Mpc and at z_{low} , hot gas traces the CW elements. Note that there is observational evidence of warm-hot gas at large scales in a filament joining Abell clusters A222 and A223 (Werner et al. 2008), where the DM component has also been detected (Dietrich et al. 2012), and more recently preliminary evidence of hot gas in cluster pairs has been found from the redMaPPer catalogue (Rykoff et al. 2014) along the sightline of a QSO by Tejos (2014), (see also his presentation in The Zeldovich Universe, Genesis and Growth of the Cosmic Web, 2014, IAU Symposium). Our results concern smaller scale structures, and they indicate that hot gas traces the CW since the moment when gas is heated at high redshift. Indeed, hot gas maps out the sites where the most violent dynamical events have occurred, such as filament, and, more particularly, node formation. Confirming warm-hot gas in filaments at different scales is a major challenge for the advance of our understanding of galaxy formation (see for example Kaastra et al. 2013, for details).

ACKNOWLEDGEMENTS

We thank Arturo Serna for allowing us to use results of simulations. We thankfully acknowledge to D. Vicente and J. Naranjo for the assistance and technical expertise provided at the Barcelona Supercomputing Centre, as well as the computer resources provided by BSC/RES (Spain). We thank DEISA Extreme Computing Initiative (DECI) for the CPU time allowed to GALFOBS project. The Centro de Computación Científica (UAM, Spain) has also provided computing facilities. This investigation was partially supported by the MICINN and MINECO (Spain) through the grants AYA2009-12792-C03-02 and AYA2012-31101 from the PNAyA, as well as by the regional Madrid V PRICIT programme through the ASTRO-MADRID network (CAM S2009/ESP-1496) and the ‘Supercomputación y e-Ciencia’ Consolider-Ingenio CSD2007-0050 project. SR thanks the MICINN and MINECO (Spain) for financial support through an FPU fellowship.

REFERENCES

- Altay G., Colberg J. M., Croft R. A. C., 2006, MNRAS, 370, 1422
- Aragón-Calvo M. A., Jones B. J. T., van de Weygaert R., van der Hulst J. M., 2007a, A&A, 474, 315
- Aragón-Calvo M. A., van de Weygaert R., Araya-Melo P. A., Platen E., Szalay A. S., 2010, MNRAS, 404, L89
- Aragón-Calvo M. A., van de Weygaert R., Jones B. J. T., 2010, MNRAS, 408, 2163
- Aragón-Calvo M. A., van de Weygaert R., Jones B. J. T., van der Hulst J. M., 2007b, ApJ, 655, L5
- Aragón-Calvo M. A., Yang L. F., 2014, MNRAS, 440, L46
- Arnold V. I., 1983, Uspekhi Mat. Nauk, 38, 77
- Bailin J., Steinmetz M., 2005, ApJ, 627, 647
- Bardeen J. M., Bond J. R., Kaiser N., Szalay A. S., 1986, ApJ, 304, 15
- Barnes J. E., 2011, MNRAS, 413, 2860
- Bell E. F., Phleps S., Somerville R. S., Wolf C., Borch A., Meisenheimer K., 2006, ApJ, 652, 270
- Bond J. R., Kofman L., Pogossyan D., 1996, Nature, 380, 603
- Bond N. A., Strauss M. A., Cen R., 2010a, MNRAS, 406, 1609
- Bond N. A., Strauss M. A., Cen R., 2010b, MNRAS, 409, 156
- Bryan G. L., Norman M. L., 1998, ApJ, 495, 80
- Buchert T., 1989, A&A, 223, 9
- Buchert T., 1992, MNRAS, 254, 729
- Buchert T., Domínguez A., 1998, A&A, 335, 395
- Buchert T., Domínguez A., 2005, A&A, 438, 443
- Buchert T., Domínguez A., Pérez-Mercader J., 1999, A&A, 349, 343
- Burgers J. M., 1948, Adv. Appl. Mech., 1, 171
- Burgers J. M., 1974, The nonlinear diffusion equation : asymptotic solutions and statistical problems. D. Reidel Pub. Co. c1974, Dordrecht-Holland, Boston, first published in 1973 under title: Statistical problems connected with asymptotic solutions of the one-dimensional nonlinear diffusion equation
- Cautun M., van de Weygaert R., Jones B. J. T., 2013, MNRAS, 429, 1286
- Cautun M., van de Weygaert R., Jones B. J. T., Frenk C. S., 2014, MNRAS, 441, 2923
- Codis S., Pichon C., Devriendt J., Slyz A., Pogossyan D., Dubois Y., Sousbie T., 2012, MNRAS, 427, 3320
- Colberg J. M., Krughoff K. S., Connolly A. J., 2005, MNRAS, 359, 272
- Coles P., Melott A. L., Shandarin S. F., 1993, MNRAS, 260, 765
- Colless M., Dalton G., Maddox S., Sutherland W., Norberg P., et al., 2001, MNRAS, 328, 1039
- Dietrich J. P., Werner N., Clowe D., Finoguenov A., Kitching T., Miller L., Simionescu A., 2012, Nature, 487, 202
- Dolag K., Meneghetti M., Moscardini L., Rasia E., Bonaldi A., 2006, MNRAS, 370, 656
- Domínguez A., 2000, Phys. Rev. D, 62, 103501
- Domínguez-Tenreiro R., Oñorbe J., Martínez-Serrano F., Serna A., 2011, MNRAS, 413, 3022
- Doroshkevich A. G., Ryaben’kii V. S., Shandarin S. F., 1973, Astrophysics, 9, 144
- Dubois Y. et al., 2014, MNRAS, 444, 1453
- Dunkley J. et al., 2009, ApJS, 180, 306
- Forero-Romero J. E., Hoffman Y., Gottlöber S., Klypin A., Yepes G., 2009, MNRAS, 396, 1815
- Franx M., Illingworth G., de Zeeuw T., 1991, ApJ, 383, 112
- Geller M. J., Huchra J. P., 1989, Science, 246, 897
- Genovese C. R., Perone-Pacifico M., Verdinielli I., Wasserman L.,

- 2012, *Journal of the American Statistical Association*, 107, 788
- Gerhard O. E., 1983, *MNRAS*, 202, 1159
- Godłowski W., Panko E., Flin P., 2011, *Acta Physica Polonica B*, 42, 2313
- González R. E., Padilla N. D., 2010, *MNRAS*, 407, 1449
- González-García A. C., Oñorbe J., Domínguez-Tenreiro R., Gómez-Flechoso M. Á., 2009, *A&A*, 497, 35
- González-García A. C., van Albada T. S., 2005, *MNRAS*, 361, 1030
- Gott, III J. R., Jurić M., Schlegel D., Hoyle F., Vogeley M., Tegmark M., Bahcall N., Brinkmann J., 2005, *ApJ*, 624, 463
- Gurbatov S. N., Malakhov A. N., Saichev A. I., 1992, *Nonlinear Random Waves and Turbulence in Nondispersive Media (Non-linear Science: Theory & Applications)*. John Wiley and Sons Ltd
- Gurbatov S. N., Saichev A. I., 1984, *Radiofizika*, 27, 456
- Gurbatov S. N., Saichev A. I., Shandarin S. F., 1989, *MNRAS*, 236, 385
- Gurbatov S. N., Saichev A. I., Shandarin S. F., 2012, *Physics Uspekhi*, 55, 223
- Hahn O., Carollo C. M., Porciani C., Dekel A., 2007a, *MNRAS*, 381, 41
- Hahn O., Porciani C., Carollo C. M., Dekel A., 2007b, *MNRAS*, 375, 489
- Hahn O., Porciani C., Dekel A., Carollo C. M., 2009, *MNRAS*, 398, 1742
- Hidding J., Shandarin S. F., van de Weygaert R., 2014, *MNRAS*, 437, 3442
- Hoffman Y., Metuki O., Yepes G., Gottlöber S., Forero-Romero J. E., Libeskind N. I., Knebe A., 2012, *MNRAS*, 425, 2049
- Huchra J. et al., 2005, in *Astronomical Society of the Pacific Conference Series*, Vol. 329, *Nearby Large-Scale Structures and the Zone of Avoidance*, Fairall A. P., Woudt P. A., eds., p. 135
- Icke V., 1973, *A&A*, 27, 1
- Jenkins A. et al., 1998, *ApJ*, 499, 20
- Jones B. J. T., van de Weygaert R., Aragón-Calvo M. A., 2010, *MNRAS*, 408, 897
- Jones D. H., Saunders W., Colless M., Read M. A., Parker Q. A., et al., 2004, *MNRAS*, 355, 747
- Kaasra J., Finoguenov A., Nicastro F., Branchini E., et al., 2013, *ArXiv e-prints*
- Kartaltepe J. S. et al., 2007, *ApJS*, 172, 320
- Kauffmann G. et al., 2003, *MNRAS*, 341, 54
- Kimm T., Devriendt J., Slyz A., Pichon C., Kassir S. A., Dubois Y., 2011, *ArXiv e-prints*
- Kirshner R. P., Oemler, Jr. A., Schechter P. L., Sackett P. A., 1981, *ApJ*, 248, L57
- Kirshner R. P., Oemler, Jr. A., Schechter P. L., Sackett P. A., 1987, *ApJ*, 314, 493
- Kitzbichler M. G., White S. D. M., 2008, *MNRAS*, 391, 1489
- Kofman L., Pogosyan D., Shandarin S., 1990, *MNRAS*, 242, 200
- Libeskind N. I., Hoffman Y., Forero-Romero J., Gottlöber S., Knebe A., Steinmetz M., Klypin A., 2013, *MNRAS*, 428, 2489
- Libeskind N. I., Hoffman Y., Knebe A., Steinmetz M., Gottlöber S., Metuki O., Yepes G., 2012, *MNRAS*, 421, L137
- Lin C. C., Mestel L., Shu F. H., 1965, *ApJ*, 142, 1431
- López-Sanjuan C. et al., 2015, *A&A*, 576, A53
- Lotz J. M., Jonsson P., Cox T. J., Primack J. R., 2010, *MNRAS*, 404, 575
- Martínez-Serrano F. J., Serna A., Domínguez-Tenreiro R., Mollá M., 2008, *MNRAS*, 388, 39
- Massey R., Rhodes J., Ellis R., Scoville N., Leauthaud A., et al., 2007, *Nature*, 445, 286
- Melott A. L., Buchert T., Weib A. G., 1995, *A&A*, 294, 345
- Melott A. L., Pellman T. F., Shandarin S. F., 1994, *MNRAS*, 269, 626
- Melott A. L., Shandarin S. F., Weinberg D. H., 1994, *ApJ*, 428, 28
- Metuki O., Libeskind N. I., Hoffman Y., Crain R. A., Theuns T., 2015, *MNRAS*, 446, 1458
- Novikov D., Colombi S., Doré O., 2006, *MNRAS*, 366, 1201
- Oñorbe J., Martínez-Serrano F. J., Domínguez-Tenreiro R., Knebe A., Serna A., 2011, *ApJ*, 732, L32
- Patton D. R., Atfield J. E., 2008, *ApJ*, 685, 235
- Patton D. R., Carlberg R. G., Marzke R. O., Pritchett C. J., da Costa L. N., Pellegrini P. S., 2000, *ApJ*, 536, 153
- Paz D. J., Stasyszyn F., Padilla N. D., 2008, *MNRAS*, 389, 1127
- Peebles P. J. E., 1980, *The large-scale structure of the universe*
- Pichon C., Pogosyan D., Kimm T., Slyz A., Devriendt J., Dubois Y., 2011, *MNRAS*, 418, 2493
- Platen E., van de Weygaert R., Jones B. J. T., 2007, *MNRAS*, 380, 551
- Pogosyan D., Bond J. R., Kofman L., Wadsley J., 1998, in *Wide Field Surveys in Cosmology*, Colombi S., Mellier Y., Raban B., eds., Editions Frontieres, Gif-sur-Yvette, France, p. 61
- Porciani C., Dekel A., Hoffman Y., 2002a, *MNRAS*, 332, 325
- Porciani C., Dekel A., Hoffman Y., 2002b, *MNRAS*, 332, 339
- Powell L. C., Bournaud F., Chapon D., Devriendt J., Gaibler V., Khochfar S., Slyz A., Teyssier R., 2013, in *IAU Symposium*, Vol. 295, *IAU Symposium*, Thomas D., Pasquali A., Ferreras I., eds., pp. 13–16
- Powell L. C., Slyz A., Devriendt J., 2011, *MNRAS*, 414, 3671
- Robaina A. R., Bell E. F., van der Wel A., Somerville R. S., Skelton R. E., McIntosh D. H., Meisenheimer K., Wolf C., 2010, *ApJ*, 719, 844
- Rykoff E. S. et al., 2014, *ApJ*, 785, 104
- Sahni V., Coles P., 1995, *Physics Reports*, 262, 1
- Serna A., Domínguez-Tenreiro R., Sáiz A., 2003, *ApJ*, 597, 878
- Shandarin S. F., Zeldovich Y. B., 1989, *Reviews of Modern Physics*, 61, 185
- Shen J., Abel T., Mo H. J., Sheth R. K., 2006, *ApJ*, 645, 783
- Sheth J. V., 2004, *MNRAS*, 354, 332
- Sheth R. K., van de Weygaert R., 2004, *MNRAS*, 350, 517
- Sousbie T., 2011, *MNRAS*, 414, 350
- Sousbie T., Colombi S., Pichon C., 2009, *MNRAS*, 393, 457
- Sousbie T., Pichon C., Colombi S., Novikov D., Pogosyan D., 2008a, *MNRAS*, 383, 1655
- Sousbie T., Pichon C., Courtois H., Colombi S., Novikov D., 2008b, *ApJ*, 672, L1
- Sousbie T., Pichon C., Kawahara H., 2011, *MNRAS*, 414, 384
- Springel V., White S. D. M., Hernquist L., 2004, in *IAU Symposium*, Vol. 220, *Dark Matter in Galaxies*, Ryder S., Pisano D., Walker M., Freeman K., eds., p. 421
- Springel V. et al., 2005, *Nature*, 435, 629
- Stoica R. S., Martínez V. J., Mateu J., Saar E., 2005, *A&A*, 434, 423
- Stoica R. S., Martínez V. J., Saar E., 2007, *Journal of the Royal Statistical Society: Series C (Applied Statistics)* 56 (4), 459–477, 56, 1
- Stoica R. S., Martínez V. J., Saar E., 2010, *A&A*, 510, A38
- Tasca L. A. M., Le Fèvre O., López-Sanjuan C., Wang P.-W., et al., 2014, *A&A*, 565, A10
- Tegmark M., Blanton M. R., Strauss M. A., Hoyle F., SDSS Collaboration, 2004, *ApJ*, 606, 702
- Tejos N., 2014, *ArXiv e-prints*

- Tempel E., Stoica R. S., Martínez V. J., Liivamägi L. J., Castellan G., Saar E., 2014, MNRAS, 438, 3465
- Tillson H., Devriendt J., Slyz A., Miller L., Pichon C., 2015, MNRAS, 449, 4363
- van de Weygaert R., Bond J. R., 2008, in Lecture Notes in Physics, Berlin Springer Verlag, Vol. 740, A Pan-Chromatic View of Clusters of Galaxies and the Large-Scale Structure, Plionis M., López-Cruz O., Hughes D., eds., p. 335
- van Haarlem M., van de Weygaert R., 1993, ApJ, 418, 544
- Van Waerbeke L., Benjamin J., Erben T., Heymans C., Hildebrandt H., et al., 2013, MNRAS, 433, 3373
- Vergassola M., Dubrulle B., Frisch U., Noullez A., 1994, A&A, 289, 325
- Weinberg D. H., Hernquist L., Katz N., 1997, ApJ, 477, 8
- Werner N., Finoguenov A., Kaastra J. S., Simionescu A., Dietrich J. P., Vink J., Böhringer H., 2008, A&A, 482, L29
- White S. D. M., Silk J., 1979, ApJ, 231, 1
- Wu Y., Batuski D. J., Khalil A., 2009, ApJ, 707, 1160
- Yepes G., Domínguez-Tenreiro R., Couchman H. M. P., 1992, ApJ, 401, 40
- Yoshisato A., Matsubara T., Morikawa M., 1998, ApJ, 498, 48
- Yoshisato A., Morikawa M., Gouda N., Mouri H., 2006, ApJ, 637, 555
- Zel'dovich Y. B., 1970, A&A, 5, 84
- Zhang Y., Yang X., Faltenbacher A., Springel V., Lin W., Wang H., 2009, ApJ, 706, 747